1

Calsyntenin-3, an atypical cadherin, suppresses inhibitory basket- and stellate-cell synapses but boosts excitatory parallel-fiber synapses in cerebellum

5

6

7

Running title: Calsyntenin-3 controls cerebellar synapse formation

9

10

Zhihui Liu[1,2*], Man Jiang[1,#], Kif Liakath-Ali[1], Jaewon Ko[3], Roger Shen Zhang[1], and

Thomas C. Südhof[1,2*]

13

[1]Department of Molecular and Cellular Physiology, and [2]Howard Hughes Medical Institute, Stanford University, Stanford, CA 94305, USA; [3]Department of Brain and Cognitive Sciences, Daegu Gyeongbuk Institute of Science and Technology, Daegu 42988, Republic of Korea

18

[#]Present address: Department of Physiology, School of Basic Medicine and Tongji Medical College, Huazhong University of Science and Technology, Wuhan 430030, China

*Correspondence: zhihuil@stanford.edu (Z.L.), tcs1@stanford.edu (T.C.S.)

ABSTRACT

Cadherins contribute to the organization of nearly all tissues, but the functions of several evolutionarily conserved cadherins, including those of calsyntenins, remain enigmatic. Puzzlingly, two distinct, non-overlapping functions for calsyntenins were proposed: As postsynaptic neurexin ligands in synapse formation, or as presynaptic adaptors for kinesin-mediated vesicular transport. Here, we show that acute CRISPR-mediated deletion of calsyntenin-3 in cerebellar Purkinje cells *in vivo* causes a large decrease in inhibitory synapses, but a surprisingly robust increase in excitatory parallel-fiber synapses. No changes in the dendritic architecture of Purkinje cells or in climbing-fiber synapses were detected. Thus, by promoting formation of an excitatory type of synapses and decreasing formation of an inhibitory type of synapses in the same neuron, calsyntenin-3 functions as a postsynaptic adhesion molecule that regulates the excitatory/inhibitory balance in Purkinje cells. No similarly opposing function of a synaptic adhesion molecule was previously observed, suggesting a new paradigm of synaptic regulation.

INTRODUCTION

Synapses mediate information transfer between neurons in brain, and process the information during transfer. In processing information, synapses are dynamic: Synapses are not only continuously restructured by various forms of synaptic plasticity, but are also eliminated and newly formed throughout life (Attardo et al., 2015; Pfeiffer et al., 2018). Synapse formation, elimination, and remodeling are thought to be organized by synaptic adhesion molecules (SAMs) (Südhof, 2021). Many candidate SAMs have been described, but most SAMs appear to make only partial contributions to the formation and specification of synapses. In particular, few SAMs were consistently found to contribute to the initial formation of synapses. At present, only adhesion-GPCR SAMs, such as latrophilins and BAIs, are known to have a major impact on synapse numbers when tested using rigorous genetic approaches (Anderson et al., 2017; Bolliger et al., 2011; Kakegawa et al., 2015; Sando et al., 2019; Sando and Sudhof, 2021; Sigoillot et al., 2015; Wang et al., 2020). In contrast, the majority of well-characterized SAMs, most prominently neurexins and LAR-type receptor phosphotyrosine phosphatases, appear to perform no major roles in establishing synaptic connections. Instead, these SAMs are essential for conferring onto synapses specific properties that differ between various types of synapses in a neural circuit (Chen et al., 2017; Emperador-Melero et al., 2021; Fukai and Yoshida, 2020; Missler et al., 2003; Sclip and Sudhof, 2020).

Calsyntenins (a.k.a. alcadeins) are atypical cadherins that are encoded by three genes in mammals (*Clstn1-3* in mice) and a single gene in Drosophila, C. elegans, and other invertebrates (Araki et al., 2003; Hintsch et al., 2002; Ohno et al., 2014; Vogt et al., 2001). Calsyntenins are type I membrane proteins containing two N-terminal cadherin domains followed by a single LNS-domain (also referred to as LG-domain), a transmembrane region, and a short cytoplasmic tail. Calsyntenins are primarily expressed in neurons, although a calsyntenin-3 (Clstn3) variant with a different non-cadherin extracellular domain is present in adipocytes (referred to as Clstn3β; Zeng et al., 2019).

Two different views of calsyntenin functions have emerged. The first view posits that calsyntenins are postsynaptic adhesion molecules that bind to presynaptic neurexins to mediate both excitatory and inhibitory synapse formation, whereas the second view

67 proposes that calsyntenins are presynaptic adaptor proteins that mediate kinesin function in
68 axonal transport. Extensive evidence supports both views.

69 In support of a role for calsynteins as a postsynaptic adhesion molecule, all calsyntenins
70 were localized by immunoelectron microscopy to the postsynaptic densities of excitatory
71 synapses in the cortex and cerebellum (Hintsch et al., 2002; Vogt et al., 2001). Moreover,
72 calsyntenins induce presynaptic specializations in heterologous synapse formation assays
73 when expressed in non-neuronal cells (Pettem et al., 2013). Most importantly, knockout
74 (KO) mice of all three calsyntenins exhibit synaptic impairments (Kim et al., 2020; Lipina et
75 al., 2016; Pettem et al., 2013; Ster et al., 2014). Careful analyses revealed that *Clstn3* KO
76 mice exhibit a 20-30% decrease in excitatory synapse density in the CA1 region of the
77 hippocampus (Kim et al., 2020; Pettem et al., 2013). In addition, Pettem et al. (2013)
78 observed a similar decrease in inhibitory synapse density, although Kim et al. (2020) failed
79 to detect the same decrease. Moreover, Pettem et al. (2013) detected a 30-40% decrease
80 in mEPSC and mIPSC frequency, but unexpectedly found no change in excitatory synaptic
81 strength as measured by input/output curves. The *Clstn2* KO also decreased the inhibitory
82 synapse density in the hippocampus approximately 10-20% (Lipina et al., 2016), whereas
83 the *Clstn1* KO modestly impaired excitatory synapses in juvenile but not in adult mice (Ster
84 et al., 2014). Viewed together, these data suggest a postsynaptic role for calsyntenins in
85 the hippocampus, although the modest effect sizes of the calsyntenin KO phenotypes were
86 puzzling. Calsyntenins were proposed to function as postsynaptic adhesion molecules by
87 binding to presynaptic neurexins, but distinct, mutually exclusive mechanisms of neurexin
88 binding were described. Pettem et al. (2013) and Lu et al. (2014) showed that the LNS
89 domain of calsyntenins binds to an N-terminal sequence of α-neurexins that is not shared
90 by β-neurexins. Kim et al. (2020), however, demonstrated that the cadherin domains of
91 calsyntenins bind to the 6th LNS domain of neurexins that is shared by α- and β-neurexins.
92 Adding to this puzzle, Um et al. (2014) did not detect direct binding of calsyntenins to
93 neurexins, and no study has reconstituted a stable calsyntenin-neurexin complex.

94 Similar to the hypothesis that calsyntenins act as postsynaptic adhesion molecules, the
95 proposal that calsyntenins function as presynaptic kinesin-adaptor proteins that facilitate
96 vesicular transport is also based on extensive studies. This proposal focuses on the
97 transport of vesicles containing APP (Araki et al., 2007; Konecna et al., 2006; Vagnoni et al.,

98   2012). A cytoplasmic sequence of calsyntenins binds to kinesins (Konecna et al., 2006),
99   and at least *Clstn1* is localized to transport vesicles containing kinesin (Ludwig et al., 2009).
100 Moreover, carefully controlled immunoprecipitations showed that calsyntenins are present
101 in a molecular complex with presynaptic GABA$_B$-receptors and APP (Dinamarca et al.,
102 2019; Schwenk et al., 2016). However, *Clstn1* KO mice exhibit only modest changes in
103 APP transport or the proteolytic processing of APP into Aβ peptides, while *Clstn2* KO mice
104 display no change (Gotoh et al., 2020). Furthermore, the *Clstn1* KO simultaneously
105 increased the levels of the C-terminal cleavage fragment (CTF) of APP and of Aβ peptides
106 without changing APP levels, making it difficult to understand how a decreased APP
107 cleavage causing increased CTF levels could also elevate Aβ levels (Gotoh et al., 2020).
108 As a result, the kinesin binding, APP interaction, and GABA$_B$-receptor complex formation by
109 calsyntenins seem well established, but it is not yet clear how these activities converge on a
110 function in axonal transport of APP.

111 The two divergent views of the function of calsyntenins, although well supported, are
112 difficult to reconcile with each other. Given the potential importance of calsyntenins, we
113 here pursued an alternative approach to study their functions. We aimed to identify neurons
114 that express predominantly one calsyntenin isoform in order to avoid potential redundancy,
115 and then examined the function of that calsyntenin isoform using acute genetic ablations
116 and synapse-specific electrophysiological analyses. Our results reveal that cerebellar
117 Purkinje cells express only *Clstn3* at high levels. Using CRISPR/Cas9-mediated deletions,
118 we unexpectedly found that the *Clstn3* KO in Purkinje cells upregulated excitatory
119 parallel-fiber synapses and had no effect on excitatory climbing-fiber synapses, but
120 suppressed inhibitory basket- and stellate-cell synapses. These results indicate that a
121 particular synaptic adhesion molecule can support formation of one class of synapses but
122 suppress formation of another class of synapses in the same neuron.

RESULTS

***Clstn3* is the predominant calsyntenin isoform in cerebellar Purkinje cells**. To analyze physiologically relevant functions of calsyntenins, we aimed to identify a type of neuron that expresses a particular calsyntenin isoform at much higher levels than others. This was necessary to avoid functional redundancy among multiple calsyntenins. Since most previous studies on calsyntenin functions were performed in the hippocampus (Kim et al., 2020; Lipina et al., 2016; Pettem et al., 2013; Ster et al., 2014), we examined calsyntenin expression in the hippocampus using single-molecule *in situ* hybridizations. All three calsyntenins were expressed in the CA1 and CA3 regions and the dentate gyrus. In the CA1 region, *Clstn1* and *Clstn3* levels were highest, in the CA3 region all three calsyntenins were similarly abundant, and in the dentate gyrus, *Clstn1* and *Clstn2* were most strongly present (Figure 1A). These results suggest that most hippocampal neurons co-express multiple calsyntenin isoforms, which may account for the modest phenotypes observed with *Clstn1*, *Clstn2*, and *Clstn3* KO mice (Kim et al., 2020; Lipina et al., 2016; Pettem et al., 2013; Ster et al., 2014).

We next examined the cerebellum because single-cell RNA transcriptome databases suggested that in the cerebellum, granule cells express primarily *Clstn1*, while Purkinje cells express *Clstn3* (Peng et al., 2019; Saunders et al., 2018; Schaum et al., 2018; Tasic et al., 2018; Zeisel et al., 2018). Indeed, single-molecule *in situ* hybridization in cerebellar sections demonstrated that the expression of calsyntenin isoforms was much more segregated in cerebellum than in the hippocampus (Figure 1B). Purkinje cells express almost exclusively *Clstn3*, although low amounts of *Clstn2* were also detectable, whereas granule cells express *Clstn1* (Figure 1C). The differential labeling signal for the calsyntenins in the cerebellum was not due to differences in probe efficiency because in the hippocampus, the same probes under the same conditions produced equally strong signals (Figure 1A). Since Purkinje cells represent an excellent experimental system for synaptic physiology, we decided to focus on the function of *Clstn3* in these neurons.

***In vivo* CRISPR efficiently deletes *Clstn3* in cerebellar Purkinje cells, causing major impairments in motor learning**. Advances in CRISPR-mediated genetic manipulations suggest that it is possible to dissect a gene's function using acute CRISPR-mediated deletions *in vivo* (Incontro et al., 2014). When we tested multiple single guide RNAs

154 (sgRNAs) for the *Clstn3* gene, we identified two sgRNAs targeting exons 2 and 3 of the

155 *Clstn3* gene that were highly efficacious in suppressing *Clstn3* expression in Purkinje cells

156 *in vivo* (Figure 2A-2G). AAVs encoding the sgRNAs and tdTomato (as an expression

157 marker) were stereotactically injected at P21 into the cerebellum of mice that constitutively

158 express *sp*Cas9 (Platt et al., 2014), and mice were analyzed at ~P50 by quantitative

159 RT-PCR (Figure 2C, 2D). The *Clstn3* CRISPR KO was highly effective, decreasing *Clstn3*

160 mRNA levels by >60% (Figure 2D, 2E). Immunoblotting confirmed the loss of ~80% of

161 *Clstn3* protein after the *Clstn3* CRISPR KO (Figure 2F). We also examined *Clstn1* and

162 *Clstn2* expression by immunoblotting, using an antibody that reacts with both isoforms and

163 additionally recognizes non-specific bands, but found no change (Figure S1). Analysis of

164 the *Clstn3* CRISPR KO for potential off-target effects demonstrated that at the sites most

165 similar to the *Clstn3* target sequence, no mutations were detected (Figure S2). Viewed

166 together, these data indicate that the cerebellar *Clstn3* CRISPR KO effectively ablates

167 *Clstn3* expression in cerebellar neurons.

168 To explore the functional consequences of the *Clstn3* KO in Purkinje cells, we analyzed its

169 effect on the motor behavior of mice. Strikingly, the cerebellar *Clstn3* KO nearly abolished

170 motor learning of the mice, as assayed with the rotarod task (Figure 2G). A behavioral test

171 measuring social interactions did not reveal significant changes (Figure S3), suggesting

172 that the mice were not broadly impaired. Thus, the *Clstn3* KO in the cerebellum likely

173 impairs cerebellar functions in a specific manner. The motor coordination deficit in *Clstn3*

174 CRISPR KO mice is consistent with phenotypes observed in constitutive *Clstn3* KO mice

175 (www.mousephenotype.org) (Dickinson et al., 2016), suggesting that our CRISPR KO

176 approach is reliable and specific.

177 **The *Clstn3* KO in Purkinje cells impairs inhibitory synapses in the cerebellar cortex.**

178 To test whether the *Clstn3* KO affected inhibitory synapses on Purkinje cells, we examined

179 the inhibitory synapse density in the cerebellar cortex using immunocytochemistry for vGAT,

180 an inhibitory synapse marker (Figure 3A). The CRISPR KO of *Clstn3* in Purkinje cells

181 robustly reduced the inhibitory synapse density in the molecular layer, Purkinje-cell layer,

182 and granule-cell layer of the cerebellar cortex (Figure 3B-3D). The most extensive decrease

183 (~60%) was observed in the deep molecular layer (Figure 3B), where we also detected a

184 significant reduction (~25%) in the size of vGAT-positive puncta (Figure 3C). vGAT-positive

185   synapses in Purkinje cell and granule cell layers were less affected (~20% reduction; Figure
186   3D).

187   The decrease in inhibitory synapse density raises the question whether inhibitory synaptic
188   transmission is suppressed. To address this question, we recorded miniature inhibitory
189   postsynaptic currents (mIPSCs) from Purkinje cells in the presence of tetrodotoxin (Figure
190   4). *Clstn3* KO produced a large decrease in mIPSC frequency (~60%), without changing
191   the mIPSC amplitude (Figure 4A-4C). Moreover, the *Clstn3* KO increased the rise but not
192   decay times of mIPSCs (Figure 4D). Measurements of the Purkinje cell capacitance and
193   input resistance showed that the Clstn3 deletion did not produce major changes,
194   demonstrating that it did not globally alter Purkinje cell properties (Figure S4A).

195   mIPSCs are heterogeneous in Purkinje cells. Smaller mIPSCs are mostly derived from
196   more distant stellate-cell synapses, and larger mIPSCs from more proximal basket-cell
197   synapses (Nakayama et al., 2012). To examine these two types of input synapses
198   separately, we plotted the mIPSC amplitudes in a normal distribution (Figure 4E). This plot
199   revealed that the majority of mIPSC amplitudes (>90%) are <60 pA. Therefore, we
200   separately analyzed mIPSCs with amplitudes of >60 pA and <60 pA, of which the >60 pA
201   mIPSCs likely represent basket cell mIPSCs, whereas the <60 pA mIPSCs are composed
202   predominantly (but not exclusively) of stellate cell mIPSCs. Both classes of mIPSCs
203   exhibited similar impairments in frequency and kinetics, although the changes were more
204   pronounced for larger mIPSCs (Figure 4F-4H; S5). These results are consistent with the
205   morphological data suggesting a larger decrease in basket cell synapses than in stellate
206   cell synapses (Figure 3A-3D).

207   Does the change in inhibitory synapse density and mIPSCs cause a change in overall
208   inhibitory synaptic strength? We examined evoked inhibitory synaptic responses, using
209   extracellular stimulations of basket cell axons close to the Purkinje cell layer (Figure 5A).
210   We detected a significant decrease (~40%) in IPSC amplitudes. The decrease in IPSC
211   amplitude is consistent with a loss of inhibitory synapses, but could also be due to a
212   decrease in release probability. However, we detected no major changes in the coefficient
213   of variation, paired-pulse ratio, or kinetics of evoked IPSCs, suggesting that the release
214   probability is normal (Figure 5B-5F, S4B). These data confirm the morphological results,
215   suggesting that the *Clstn3* KO decreases inhibitory synapse numbers.

***Clstn3* deletion in Purkinje cells increases excitatory parallel-fiber but not climbing-fiber synapse densities**. The decrease in inhibitory synapse numbers by the *Clstn3* KO is consistent with previous studies suggesting that *Clstn3* promotes synapse formation in the hippocampus, but these previous studies primarily identified a decrease in excitatory synapses (Kim et al., 2020; Pettem et al., 2013; Ranneva et al., 2020). We thus tested whether the *Clstn3* KO also affects excitatory synapse numbers in cerebellum. Purkinje cells receive two different excitatory synaptic inputs with distinct properties: Parallel-fiber synapses that are formed by granule cells on distant Purkinje cell dendrites, and climbing-fiber synapses that are formed by inferior olive neurons on proximal Purkinje cell dendrites. Parallel-fiber synapses use the vesicular glutamate transporter vGluT1, whereas climbing-fiber synapses use the vesicular glutamate transporter vGluT2 (Hioki et al., 2003). Moreover, parallel-fiber synapses are surrounded by processes formed by Bergmann astroglial cells, creating a tripartite synapse in which the glial processes contain high levels of GluA1 (Baude et al., 1994). As a first step towards assessing the effect of the *Clstn3* KO on excitatory synapses on Purkinje cells, we analyzed cerebellar sections from control and *Clstn3* KO mice by immunohistochemistry for vGluT1, vGluT2 and GluA1 (Figure 6).

Confocal microscopy of cerebellar cortex sections immunolabeled for vGluT1 revealed intense staining that, surprisingly, was enhanced by the *Clstn3* deletion in Purkinje cells (Fig. 6A). Because parallel-fiber synapses in the cerebellar cortex are so numerous that confocal microscopy cannot resolve individual vGluT1-positive synaptic puncta, we measured the overall vGluT1 staining intensity as a proxy for synapse density (Figure 6A) (Zhang et al., 2015). The *Clstn3* deletion in Purkinje cells caused a robust increase (~25%) in the vGluT1 staining intensity of both the superficial and the deep molecular layers of the cerebellar cortex (Figure 6B).

The potential increase in parallel-fiber synapses induced by the *Clstn3* KO, suggested by the enhanced vGluT1 staining intensity, is unexpected. This prompted us to examine the levels of GluA1 as an astroglial marker of tripartite parallel-fiber synapses (Figure 6C; Baude et al., 1994). Again, the *Clstn3* KO in Purkinje cells induced a significant increase (~25%) in synaptic GluA1 staining intensity (Figure 6D), consistent with the increase in vGluT1 staining intensity.

247   We next analyzed the density of climbing-fiber synapses by staining cerebellar sections for

248   vGluT2, but detected no significant effect of the *Clstn3* KO in Purkinje cells (Figure 6E).

249   Different from parallel-fiber synapses that contain vGluT1, climbing-fiber synapses are

250   labeled with antibodies to vGluT2 and are readily resolved by confocal microscopy (Figure

251   6E). The number and size of synaptic puncta identified with vGluT2 antibodies were not

252   altered by the *Clstn3* KO, although there was a slight trend towards a decrease in

253   climbing-fiber synapse density (Figure 6F, 6G). These observations suggest that the

254   enhancement of parallel-fiber synapse density by the *Clstn3* KO is specific for this type of

255   synapse.

256   **The *Clstn3* KO increases the spine density of Purkinje cells**. It is surprising that the

257   *Clstn3* KO in Purkinje cells appears to increase the parallel-fiber synapse density, as one

258   would expect a synaptic adhesion molecule to promote but not to suppress formation of a

259   particular synapse. The parallel-fiber synapse increase is likely not a homeostatic response

260   to the loss of inhibitory synapses because such a response, which would aim to maintain

261   the correct excitatory/inhibitory balance, should involve a decrease, and not an increase, in

262   parallel-fiber synapses. The increase in parallel-fiber synapse numbers is also unexpected

263   given previous results showing that in hippocampal CA1 neurons, the *Clstn3* KO decreases

264   excitatory synapse numbers (Kim et al., 2020; Pettem et al., 2013). To independently

265   confirm this increase, we analyzed the dendritic spine density in Purkinje cells. Since nearly

266   all spines contain parallel-fiber synapses and all parallel-fiber synapses are on spines

267   (Sotelo, 1975), the spine density of Purkinje cells represents a reliable proxy for synapse

268   density.

269   We filled individual Purkinje cells in acute slices with biocytin via a patch-pipette, and

270   analyzed their dendritic structure and spine density by quantitative morphometry (Figure 7A,

271   S6A, S6B). Reconstructions of 6 Purkinje cells from control and *Clstn3* KO mice revealed a

272   trend towards an increased dendrite length in *Clstn3*-deficient Purkinje cells without a

273   significant change in dendritic architecture, demonstrating that the *Clstn3* KO does not

274   impair the overall structure of Purkinje cells (Figure 7B). Quantification of dendritic spines

275   uncovered in *Clstn3*-deficient Purkinje cells a robust increase (~30%) in the density of

276   spines in the superficial area of the cerebellar cortex, and a trend towards an increase in

277   the deep area of the cerebellar cortex (Figure 7C-7F). The increase in spine density was

278 particularly pronounced for thin spines (Figure 7G; S6C, S6D). These findings provide
279 independent evidence that the *Clstn3* KO increases the parallel-fiber synapse density, and
280 precisely mirror those obtained by analyzing the vGluT1- and GluA1-staining intensity of the
281 cerebellar cortex (Figure 6A-6D).

282 **The *Clstn3* KO increases parallel-fiber but not climbing-fiber synaptic transmission**.
283 The increase in parallel-fiber synapses could be due to a true enhancement of parallel-fiber
284 synapse formation, or a compensatory reaction to a decrease in parallel-fiber synapse
285 function. Although the latter hypothesis would be consistent with a homeostatic response, it
286 seems unlikely given that in vertebrates, synapses rarely proliferate in response to a
287 functional impairment. To clarify this question, we analyzed parallel-synapse function by
288 electrophysiology, and compared it to climbing-fiber synapse function as an internal control
289 since climbing-fiber synapse numbers are not changed by the *Clstn3* KO in Purkinje cells.

290 We first monitored spontaneous miniature synaptic events (mEPSCs) in the presence of
291 tetrodotoxin. We observed an increase in mEPSC amplitudes (~25%) and frequency (~15%)
292 in *Clstn3* KO neurons, without a notable change in mEPSC kinetics (Figure 8A-8D). Most
293 mEPSCs in Purkinje cells are derived from parallel-fiber synapses. Because of the large
294 dendritic tree of Purkinje cells, synapses on distant dendrites produce slower and smaller
295 mEPSCs than synapses on proximal dendrites (Zhang et al., 2015). To ensure that we
296 were monitoring mEPSCs derived from parallel-fiber synapses (whose density is increased
297 morphologically), we analyzed only slow mEPSCs with rise times of >1 ms that are mostly
298 generated by parallel-fiber synapses on distant dendrites (Nakayama et al., 2012;
299 Yamasaki et al., 2006). The results were the same as for total mEPSCs, confirming that the
300 *Clstn3* KO increases parallel-fiber synaptic activity (Figure 8E-8H).

301 Finally, we measured evoked parallel-fiber EPSCs, using input-output curves to correct for
302 variations in the placement of the stimulating electrode (Figure 9A). Consistent with the
303 morphological and mEPSC data, the *Clstn3* KO robustly enhanced parallel-fiber synaptic
304 responses (~60% increase) (Figure 9B-9D). This finding suggests that the *Clstn3* KO not
305 only increases the density of parallel-fiber synapses, but also renders these synapses more
306 efficacious. The increased strength of parallel-fiber synaptic transmission was not due to a
307 change in release probability because neither the coefficient of variation nor the
308 paired-pulse ratios of parallel-fiber EPSCs were affected (Figure 9E-9G). The increase of

309 parallel-fiber EPSCs is consistent with the vGluT1 intensity and mEPSC amplitude changes,

310 providing further evidence that the *Clstn3 KO* enhances parallel-fiber synapses.

311 In contrast to parallel-fiber EPSCs, climbing-fiber EPSCs exhibited no *Clstn3* KO-induced

312 alteration. Specifically, the amplitude, paired-pulse ratio, and kinetics of climbing-fiber

313 EPSCs in control and *Clstn3* KO Purkinje cells were indistinguishable (Figure 9H-9L).

314 These findings are consistent with the lack of a change in vGluT2-positive synaptic puncta

315 analyzed morphologically (Figure 6E-6G). Viewed together, these data suggest that *Clstn3*

316 *KO* produces an increase in excitatory parallel-fiber, but not climbing-fiber, synapses.

317

318 **DISCUSSION**

319 Calsyntenins are intriguing but enigmatic cadherins, a class of diverse adhesion molecules

320 that generally function as tissue organizers. Two distinct, non-overlapping roles were

321 proposed for calsyntenins, as a postsynaptic adhesion molecule promoting synapse

322 formation and as a kinesin-adaptor protein mediating axonal and dendritic transport, in

323 particular of APP (Araki et al., 2007; Kim et al., 2020; Konecna et al., 2006; Lipina et al.,

324 2016; Pettem et al., 2013; Ster et al., 2014; Vagnoni et al., 2012). Both functions are

325 supported by extensive data, but neither function was conclusively tested. Here, we

326 examined the role of one particular calsyntenin, *Clstn3*, in one particular neuron, Purkinje

327 cells that predominantly express this calsyntenin isoform. Our data establish that *Clstn3*

328 acts as a postsynaptic adhesion molecule in Purkinje cells that is selectively essential for

329 regulating synapse numbers, confirming an essential function for *Clstn3* as a synaptic

330 adhesion molecule. Our data are surprising in revealing that *Clstn3* functions not by

331 universally promoting synapse formation, but by exerting opposite effects in different types

332 of synapses. Specifically, our results demonstrate that deletion of *Clstn3* causes a

333 decrease in inhibitory basket- and stellate-cell synapses on Purkinje cells, but an increase

334 in excitatory parallel-fiber synapses (Figure S7). Thus, *Clstn3* doesn't function simply as a

335 synaptogenic adhesion molecule, but as a regulator of the balance of excitatory and

336 inhibitory synaptic inputs on Purkinje cells.

337 The functions we describe here for *Clstn3* are different from those of previously identified

338 synaptic adhesion molecules or synapse-organizing signals. Whereas presynaptic

339 adhesion molecules generally act in both excitatory and inhibitory synapses, few

340   postsynaptic adhesion molecules were found to function in both. In the rare instances in
341   which an adhesion molecule was documented to mediate signaling in excitatory and
342   inhibitory synapses, such as the case of *Nlgn3* (but not of other neuroligins), it acts to
343   promote synaptic function in both (Chanda et al., 2017; Zhang et al., 2015). Not only do we
344   find that *Clstn3*, different from previously identified synaptic adhesion molecules, restricts
345   formation at a specific synapse (parallel-fiber synapses), but also that *Clstn3* enhances
346   formation of another specific synapse (GABAergic basket- and stellate-cell synapses) in the
347   same neurons.

348   Several questions arise. First, why are the phenotypes we observe in *Clstn3* KO Purkinje
349   cells so much stronger than those previously detected in CA1-region pyramidal neurons
350   (Kim et al., 2020; Pettem et al., 2013)? This difference could be due to differences in cell
351   type or to the more acute nature of our manipulations. More likely, however, this
352   difference is caused by the lack of redundancy of *Clstn3* function in Purkinje cells since
353   other calsyntenin isoforms are co-expressed with *Clstn3* in CA1-region neurons (Figure 1A),
354   but not in Purkinje cells (Figure 1B, 1C).

355   Second, what is the mechanism of *Clstn3* action at synapses? We used manipulations in
356   young adult mice in which cerebellar synapses are not yet completely established and in
357   which synapse formation and elimination likely occurs continuously (Attardo et al., 2015;
358   Pfeiffer et al., 2018). At present, our data do not reveal whether *Clstn3* acts in the initial
359   establishment and/or the maintenance of synapses, a somewhat artificial distinction since
360   synapse formation may actually consist in the stabilization of promiscuous contacts and
361   synapses turn over continuously (Südhof, 2021). The functional consequences of these
362   actions for cerebellar circuits are identical, in that both lead to a dramatic shift in
363   excitatory/inhibitory balance in the cerebellar cortex.

364   Third, what trans-synaptic interactions mediate the functions of *Clstn3*? Several papers
365   describe binding of calsyntenins to neurexins (Kim et al., 2020; Pettem et al., 2013).
366   However, our data uncover a phenotype that is different from that observed with deletions
367   of neurexins or neurexin ligands, suggesting that *Clstn3* does not function exclusively by
368   binding to neurexins. The deletion of the neurexin ligand Cbln1 leads to a loss of
369   parallel-fiber synapses in the cerebellar cortex instead of a gain, suggesting that a different
370   calsyntenin ligand is involved. Moreover, the specific conclusions of the papers describing

calsyntenin-binding to neurexins differ (Kim et al., 2020; Pettem et al., 2013), leaving the interaction mode undefined. Thus, we believe the most parsimonious hypothesis is that postsynaptic calsyntenins function by binding to presynaptic ligands other than neurexins that remain to be identified.

Fourth, does *Clstn3* physiologically act to restrict the formation of excitatory parallel-fiber synapses, leading to an increase in parallel-fiber synapses upon deletion of *Clstn3*, or is this increase an indirect compensatory effect produced by the decrease in inhibitory synapses? Multiple arguments support a specific action of *Clstn3* at parallel-fiber synapses. *Clstn3* protein was localized to parallel-fiber synapses by immunoelectron microscopy (Hintsch et al., 2002). Moreover, other genetic manipulations that cause a decrease in inhibitory synaptic transmission in cerebellar cortex, such as deletions of *Nlgn2* or of GABA$_A$-receptors (Briatore et al., 2020; Fritschy et al., 2006; Meng et al., 2019; Zhang et al., 2015), do not induce an increase in excitatory parallel-fiber synapses. Finally and probably most importantly, although competition between synapses using the same transmitters is well-described (e.g., competition between glutamatergic parallel- and climbing-fiber synapses on Purkinje cells; Cesa and Strata, 2009; Miyazaki et al., 2012; Strata et al., 1997), no such competition has been observed between GABAergic and glutamatergic synapses, such that the decrease in one of them would lead to the increase of the other. Quite the contrary, the rules of homeostatic plasticity would predict that a decrease in GABAergic synapses should lead to a decrease, not an increase, in glutamatergic synapses (Monday et al., 2018; Nelson and Valakh, 2015). Thus, our data overall suggest that *Clstn3* specifically acts to limit the formation of parallel-fiber synapses and enhance the formation of inhibitory synapses in the cerebellar cortex.

Our study also has clear limitations. We did not examine axonal or dendritic transport, and cannot exclude the possibility that *Clstn3* performs an additional function as an adaptor for kinesin-mediated transport. Moreover, we cannot rule out the possibility that different calsyntenins perform distinct functions. In addition, although the postsynaptic functions of *Clstn3* in Purkinje cell synapses strongly argue against a neurexin-dependent mechanism, our data do not exclude the possibility that calsyntenins perform other functions in other neurons in a neurexin-dependent manner. The example of neuroligins shows that a

401   synaptic adhesion molecule can have both a neurexin-dependent and
402   neurexin-independent functions (Ko et al., 2009; Wu et al., 2019).

403   Multiple synaptic adhesion molecules have already been implicated in synapse formation in
404   Purkinje cells. The interaction of presynaptic neurexins with cerebellins and postsynaptic
405   GluD receptors plays a major role in shaping parallel-fiber synapses (Yuzaki and Aricescu,
406   2017), and the binding of C1ql1 to postsynaptic Bai3 has a prominent function in
407   climbing-fiber synapses (Kakegawa et al., 2015; Sigoillot et al., 2015). Postsynaptic *Nlgn2*
408   and *Nlgn3* are major contributors to the function of GABAergic synapses in Purkinje cells
409   (Zhang et al., 2015), as is dystroglycan (Briatore et al., 2020). How can we envision the
410   collaboration of various synaptic adhesion complexes in establishing and shaping the
411   different types of synapses on Purkinje cells? Do these molecules act sequentially at
412   different stages, collaborate, or work in parallel? The overall view of synapse formation that
413   emerges from these studies resembles a conductorless orchestra, in which different
414   players individually contribute distinct essential facets to the work that is being performed.
415   In this orchestra, some players, such as neurexins, play prominent roles in coordinating the
416   actions of their sections, whereas others, such as latrophilins, initiate movements. In this
417   scenario, *Clstn3* (and possibly other calsyntenins) may regulate the loudness of different
418   sections of the orchestra, or translated into the terms of a synapse, control the efficacy of
419   signals regulating excitatory vs. inhibitory synapses.

420 **METHODS**

421 **Key resources table**

Reagent type (species) or resource	Designation	Source or reference	Identifiers	Additional information
Genetic reagent (Mus musculus)	Constitutive Cas9	PMID: 25263330	JAX ID: 024858	
Cell line (Homo sapiens)	HEK293T	ATCC	CRL-11268	
Recombinant DNA reagent	AAV-U6-sg66-U6-sg21-CAG tdTomato	This paper		Serotyped with AAV-DJ
Sequencebased reagent	Clstn1 RNA FISH probe	Advanced Cell Diagnostics	Cat: 542611	
Sequencebased reagent	Clstn2 RNA FISH probe	Advanced Cell Diagnostics	Cat: 542621	
Sequence based reagent	Clstn3 RNA FISH probe	Advanced Cell Diagnostics	Cat: 542631	
Sequence based reagent	Clstn3 qPCR primers and probe	This paper		
Antibody	Anti-pan Clstn1/2 rabbit polyclonal	PMID: 24613359		1:1000 IB
Antibody	Clstn3 rabbit polyclonal	PMID: 24613359		1:1000 IB
Antibody	Anti-ACTB mouse monoclonal	Sigma	#A1978	1:10000 IB
Antibody	IRDye® 680LT Donkey anti-Rabbit	LI-COR	926-68023	1:10000 IB
Antibody	IRDye® 800CW donkey anti-mouse	LI-COR	926-32212	1:10000 IB

Antibody	Anti-vGluT1 rabbit polyclonal	Yenzym	YZ6089	1:1000 IHC
Antibody	Anti-vGluT2 rabbit polyclonal	Yenzym	YZ6097	1:1000 IHC
Antibody	Anti-vGAT guinea pig polyclonal	Sysy	131004	1:1000 IHC
Antibody	Alexa goat anti guinea pig 633	Invitrogen	A-21105	1:1000 IHC
Antibody	Alexa goat anti rabbit 647	Invitrogen	A-21245	1:1000 IHC
Chemical compound, drug	Tribromoethanol	Sigma	T48402	250 mg/kg for anesthesia
Chemical compound, drug	Picrotoxin	Tocris	1128	
Chemical compound, drug	APV	Tocris	0106	
Chemical compound, drug	CNQX	Tocris	1045	
Chemical compound, drug	NBQX	Tocris	1044	
Chemical compound, drug	Tetrodotoxin	Cayman Chemical	14964	
Chemical compound, drug	DAPI	Sigma	D8417	
Chemical compound, drug	Biocytin	Sigma	B4261	
Software, algorithm	SnapGene	GSL Biotech		previously existing
Software, algorithm	Image Studio Lite	LI-COR		previously existing
Software, algorithm	pClamp10	Molecular Device		previously existing
Software, algorithm	Clampfit10	Molecular Device		previously existing
Software, algorithm	NIS-Elements AR	Nikon		previously existing
Software, algorithm	ImageJ	National Institutes of Health		previously existing
Software, algorithm	Neurolucida360	MBF science		previously existing

Software, algorithm	Adobe Illustrator	Adobe		previously existing
Software, algorithm	Graphpad Prism 8.0	Graphpad software		previously existing

422 IB: immunoblotting, IHC: immunohistochemistry

423

424 **Animals**

425 Constitutive Cas9 mice (https://www.jax.org/strain/024858) were used and maintained as

426 homozygotes (Platt et al., 2014). Analyses were performed on littermate mice. Mice were

427 fed ad libitum and on 12 hour light dark cycles. All protocols were carried out under National

428 Institutes of Health *Guidelines for the Care and Use of Laboratory Animals* and were

429 approved by the Administrative Panel on Laboratory Animal Care at Stanford University.

430

431 **Single molecule RNA fluorescent in-situ hybridization (smRNA-FISH)**

432 smRNA-FISH in-situ hybridization experiment was performed on brain sections from P30

433 wild type C57BL/6J mice according to the manufacturer instructions using Multiplex

434 Fluorescent Detection Reagents V2 kit (# 323110, Advanced Cell Diagnostics).

435 Predesigned probes for Clstn1 (# 542611), Clstn2 (# 542621), and Clstn3 (# 542631) were

436 purchased from ACD.

437

438 **SgRNA design and generation of Vectors**

439 SgRNAs were designed using protocols developed by the Zhang lab

440 (https://zlab.bio/guide-design-resources) to minimize potential off-target effects. The pAAV

441 construct was modified from Addgene #60231 (Platt et al., 2014) with Cre-GFP replaced by

442 tdTomato and human synapsin by CAG promoter to allow efficient expression in the

443 cerebellum. Two sgRNAs were cloned in a single vector using Golden Gate Cloning

444 assembly. Empty vector without sgRNAs was used as control. Genome editing efficiency of

445 sgRNAs was initially evaluated using TIDE (https://tide.nki.nl/) (Brinkman et al., 2014).

446 Potential off-target editing sites were chosen from predictions while design. Forward and

447 reverse primers were designed to flank sgRNAs, and PCR product of Genomic DNA were

448 sequenced and compared on TIDE.

449 Primers for off-target site sequencing on sg66:

Chromosome	Forward primer	Reverse primer
chr7	GAACCCCAAGTACGCCAAGA	TTGACAGTGTGTGGCTGTGT
chr2	TGCTCCGAGGTCTCCCTAAA	AAGGTTCCAGGTCCTGTTGC
chr13	AAGAGATCCCTCCGAACATGG	GCCCATCTGACAGGAGTATGT

450

451 Primers for off-target site sequencing on sg21:

Chromosome	Forward primer	Reverse primer
chr17	GGCAGATCTCTCGTGATGGC	TTAGTCTTGGCTGCGTCACC
chr5	GGAACAAAAGCCTGGCTCC	AATCTGGGCTGGCTCATTCC
chr13	AGAGAAGGGAATGGGACCGA	ATGGCTCAGCGATTAGTGGG

452

AAV preparation and stereotactic Injections

454 pAAV carrying sgRNAs was serotyped with the AAV-DJ capsid (Grimm et al., 2008). Briefly,
455 helper plasmids (phelper and pDJ) and AAV-sgRNA vector were co-transfected into
456 HEK293T cells (ATCC, CRL-11268), at 4 μg of each plasmid per 30 cm^2 culture area, using
457 the calcium phosphate method. Cells were harvested 72 h post-transfection, and nuclei
458 were lysed and AAVs were extracted using a discontinuous iodixanol gradient media at
459 65,000 rpm for 3 h. AAVs were then washed and dialyzed in DMEM and stored at -80 ℃
460 until use. Genomic titer was tested with qPCR and adjusted to 5 x 10^{12} particles/ml for *in*
461 *vivo* injections.

462 P21 Cas9 mice were anesthetized with tribromoethanol (250 mg/kg, T48402, Sigma, USA),
463 head-fixed with a stereotaxic device (KOPF model 1900). AAVs carrying sgRNAs or control
464 viruses were loaded via a glass pipette connected with a 10 μl Hamilton syringe (Hamilton,
465 80308, US) on a syringe injection pump (WPI, SP101I, US) and injected at a speed of 0.15
466 μl/min. Pipette was left in cerebellum for additional 5 min after injection completion.
467 Carprofen (5 mg/kg) was injected subcutaneously as anti-analgesic treatment. To infect the
468 whole cerebellum, we injected multiple sites evenly distributing over the cerebellum skull,
469 coordinates were as previously reported (Zhou et al., 2020), anterior to bregma, lateral to
470 midline, ventral to dura (mm): (–5.8,±0.75), (–5.8, ±2.25), (–6.35, 0), (–6.35, ±1.5), (–6.35,

471   ±3), (–7, ±0.75), and (–7, ±2.25), with a series of depth (mm): 2, 1.5, 1, 0.5, and volume was

472   0.3 µl/depth. Viruses were coded during virus injection and remained blinded throughout

473   the whole study until data analyses were done.

474

475   **Quantitative RT-PCR**

476   Virus-infected cerebellar tissue indicated by tdTomato was carefully dissected under

477   fluorescence microscope. RNA was extracted using Qiagen RNeasy Plus Mini Kit with the

478   manufacturer's protocol (Qiagen, Hilden, Germany). Quantitative RT-PCR was run in

479   QuantStudio 3 (Applied biosystems, Thermo Fisher Scientific, USA) using TaqMan Fast

480   Virus 1-Step Master Mix (PN4453800, Applied biosystems, Thermo Fisher Scientific, USA).

481   PrimerTime primers and FAM-dye coupled detection probes were used for detecting Clstn3

482   mRNA level. To detect genome editing efficiency, qPCR primers and probe were targeting

483   the two exons and designed to flank the double-strand breaks of the two sgRNAs (Yu et al.,

484   2014). (Clstn3: Forward primer: AGAGTACCAGGGCATTGTCA; reverse primer:

485   GATCACAGCCTCGAAGGGTA; probe: TGGATAAAGATGCTCCACTGCGCT). A

486   commercially-available GAPDH probe was used as internal control (Cat: 4352932E,

487   Applied Biosystems).

488

489   **Immunohistochemistry**

490   Immunohistochemistry on the cerebellar cortex was done as previously reported (Zhang et

491   al., 2015). Mice were anesthetized with isoflurane and sequentially perfused with

492   phosphate buffered saline (PBS) and ice cold 4% paraformaldehyde (PFA). Brains were

493   dissected and post-fixed in 4% PFA overnight, then cryoprotected in 30% sucrose in PBS

494   for 24 h. 40 µm thick sagittal sections of cerebellum were collected using a Leica

495   CM3050-S cryostat (Leica, Germany). Free floating brain sections were incubated with

496   blocking buffer (5% goat serum, 0.3% Triton X-100) for 1 h at room temperature, then

497   treated with primary antibodies diluted in blocking buffer overnight at 4 ℃ (anti-vGluT1,

498   Rabbit, YZ6089, Yenzym, 1:1,000; anti-vGluT2, Rabbit, YZ6097, 1:1,000, Yenzym;

499   anti-vGAT, guinea pig, 131004, Sysy,1:1,000). Sections were washed three times with PBS

500   (15 min each), then treated with secondary antibodies (Alexa goat anti guinea pig 633,

501 A-21105, Invitrogen, 1:1,000; or Alexa goat anti rabbit 647, A-21245, Invitrogen, 1:1,000)

502 for 2 h at room temperature. After washing with PBS 4 times (15 min each), sections were

503 stained with DAPI (D8417, Sigma) and mounted onto Superfrost Plus slides with mounting

504 media. Confocal images were acquired with a Nikon confocal microscope (A1Rsi, Nikon,

505 Japan) with 60x oil objective, at 1024 x 1024 pixels, with z-stack distance of 0.3 μm. All

506 acquisition parameters were kept constant within the same day between control and Clstn3

507 KO groups. Images were taken from cerebellar lobules IV/V. Images were analyzed with

508 Nikon analysis software. During analysis, we divided the cerebellar cortex into different

509 layers to compare *Clstn3* KO effects. We defined 0-40% as superficial molecular layer and

510 40-80% as molecular deep layers, 80-100% as PCL, and we analyzed and labeled GCL

511 separately in vGAT staining.

512

513 **Immunoblotting**

514 Immunoblotting was performed as described previously (Zhang et al., 2015). Mice were

515 anesthetized with isoflurane and decapitated on ice, with the cerebellum dissected out and

516 homogenized in RIPA buffer (in mM: 50 Tris-HCl pH7.4, 150 NaCl, 1% Triton X-100, 0.1%

517 SDS, 1 EDTA) with protease inhibitor cocktail (5056489001, Millipore Sigma) and kept on

518 ice for 30 min. Samples were centrifuged at 14,000 rpm for 20 min at 4 ℃, supernatant

519 were kept and stored in -80 ℃ until use. Proteins were loaded onto 4-20% MIDI Criterion

520 TGX precast SDS-PAGE gels (5671094, Bio-Rad), and gels were blotted onto

521 nitrocellulose membranes using the Trans-blot turbo transfer system (Bio-Rad).

522 Membranes were blocked in 5% milk diluted in PBS for 1 h at room temperature, then

523 incubated overnight at 4 ℃ with primary antibodies diluted in 5% milk in TBST (0.1%

524 Tween-20). Primary antibodies of anti-Clstn3 (Rabbit, 1:1,000) and anti-pan Clstn1 and 2

525 (Rabbit, 1:1,000) were previously described (Um et al., 2014). Antibody against beta-actin

526 from Sigma (A1978, Mouse, 1:10,000) was used as a loading control.

527 Membranes were then washed with TBST and incubated with fluorescence labeled IRDye

528 secondary antibodies (IRDye® 680LT Donkey anti-Rabbit, 926-68023, LI-COR, 1:10,000;

529 IRDye® 800CW donkey anti-mouse, 926-68023, LI-COR, 1:10,000). Signals were detected

530 with Odyssey CLx imaging systems (LI-COR) and data were analyzed with Image Studio

531 5.2 software. Total intensity values were normalized to actin prior to control.

532

533 **Electrophysiology**

534 Cerebellar electrophysiology was carried out as described previously (Caillard et al., 2000;

535 Foster and Regehr, 2004; Llano et al., 1991; Zhang et al., 2015). Briefly, the cerebellum

536 was rapidly removed and transferred into continuously oxygenated ice cold cutting

537 solutions (in mM: 125 NaCl, 2.5 KCl, 3 MgCl$_2$, 0.1 CaCl$_2$, 25 glucose, 1.25 NaH$_2$PO$_4$, 0.4

538 ascorbic acid, 3 myo-inositol, 2 Na-pyruvate, and 25 NaHCO$_3$). 250 μm sagittal slices were

539 cut using a vibratome (VT1200S, Leica, Germany) and recovered at room temperature for

540 $>$1 h before recording. Oxygenated ACSF (in mM: 125 NaCl, 2.5 KCl, 1 MgCl$_2$, 2 CaCl$_2$, 25

541 glucose, 1.25 NaH$_2$PO$_4$, 0.4 ascorbic acid, 3 myo-inositol, 2 Na-pyruvate, and 25 NaHCO$_3$)

542 was perfused at 1 ml/min during recording. Whole cell recordings with Purkinje cells were

543 from cerebellar lobules IV/V, with patch pipettes (2-3 MΩ) pulled from borosilicate pipettes

544 (TW150-4, WPI, USA) using PC-10 puller (Narishige, Japan). The following internal

545 solutions were used (in mM): (1) for EPSC, 140 CsMeSO$_3$, 8 CsCl, 10 HEPES, 0.25 EGTA,

546 2 Mg-ATP, 0.2 Na-GTP (pH adjusted to 7.25 with CsOH); (2) for IPSC, 145 CsCl, 10

547 HEPES, 2 MgCl$_2$, 0.5 EGTA, 2 Mg-ATP, 0.2 Na-GTP (pH adjusted to 7.25 with CsOH).

548 Liquid junction was not corrected during all recordings. For all EPSC recordings, 50 μM

549 picrotoxin (1128, Tocris) and 10 μM APV (0106, Tocris) were contained in ACSF, and (1)

550 additionally 0.5 μM NBQX (1044, Tocris) were included for climbing-fiber EPSC recordings;

551 (2) 1 μM TTX (Tetrodotoxin, 14964, Cayman Chemical) for mEPSC recordings. For all

552 IPSC recordings, (1) 10 μM CNQX (1045, Tocris) and 10 μM APV were included in ACSF,

553 and (2) 1 μM TTX were included in mIPSC recordings. A glass theta electrode (64-0801,

554 Warner Instruments, USA, pulled with PC-10) filled with ACSF was used as stimulating

555 electrode, and littermate control and Clstn3 knockout mice were analyzed meanwhile using

556 the same stimulating electrode. For climbing fibers, the electrode was placed in the granule

557 cell layer around Purkinje cells and identified by all-or-none response, together with

558 paired-pulse depression at 50 ms inter-stimulus interval (Eccles et al., 1966; Zhang et al.,

559 2015). For parallel fibers, electrodes were placed in distal molecular layer with the same

560 distance for both control and Clstn3 knockout mice (~200 μm from the recorded Purkinje

561   cell) and identified by paired-pulse facilitation at 50 ms inter-stimulus interval (Zhang et al.,

562   2015). For basket cell stimulations, electrodes were placed in the proximal molecular layer

563   (within~100 µm from the recorded Purkinje cell) and also identified with all-or-none

564   response (Caillard et al., 2000; Zhang et al., 2015). Cells with >20% changes in series

565   resistances were rejected for further analysis. All electrophysiological data were sampled

566   with Digidata1440 (Molecular Device, USA) and analyzed with Clampfit10.4. Coefficient of

567   variation was calculated according to previous report (Lisman et al., 2007).

568

569   Biocytin labeling in Purkinje cells

570   2 mg/ml Biocytin (B4261, Sigma) was dissolved in Cs-methanesulfonate internal solution

571   followed by whole-cell voltage clamp recordings in the Purkinje cells (Sando et al., 2019).

572   Slices were fixed in 4% PFA/PBS solution overnight at 4℃. Slices were then washed 3 X 5

573   mins with PBS, permeabilized, and blocked in 5% goat serum, 0.5% Triton-X100 in PBS at

574   room temperature for 1 h. Then slices were incubated in 1:1,000 diluted Streptavidin

575   Fluor™ 647 conjugate (S21374, Invitrogen) at room temperature for 2 h in 5% goat serum

576   in PBS, washed 5 X 5 min with PBS, and mounted onto Superfrost Plus slides for imaging.

577   Image overviews were obtained with a Nikon confocal microscope (A1Rsi, Nikon, Japan)

578   with a 60x oil objective, at 1024 x 1024 pixels, with z-stack distance of 2 µm. Dendritic tree

579   3D reconstructions were performed using Neurolucida360 software (MBF science, USA) in

580   the Stanford Neuroscience Microscopy Service Center. Note that some somas could not be

581   detected automatically and were manually labeled. Spine images were obtained with a

582   ZESS LSM980 inverted confocal, Airyscan2 for fast super-resolution setup, equipped with

583   an oil-immersion 63X objective. Z-stacks were collected at 0.2 µm intervals at 0.06 µm/pixel

584   resolution with Airyscan2. Spine images were deconvolved using ZEN blue software

585   (ZESS). Spine density and characteristics were analyzed with Neurolucida360 software

586   (MBF science, USA) in Stanford Neuroscience Microscopy Service Center. Only last order

587   dendrites were analyzed, with 5-8 dendrites per cell per layer.

588

589   Behavior

590 *Accelerating rotarod.* Mice were placed on an accelerating rotarod (IITC Life Science). The

591 rod accelerated from 4 to 40 r.p.m. in 5 min. Mice were tested 3 times per day with 1 hour

592 interval and repeated for 3 days. Time stayed on the rod was recorded while the mouse fell

593 off, or hanged on without climbing, or reached 5 min.

594 *Three-chamber social interaction.* Social interaction was evaluated in a three-chamber box.

595 Mice were placed initially in the central chamber to allow 10 min habituation for all three

596 chambers. For sociability session, a same sex- and age matched stranger mouse

597 (stranger1) was placed inside an upside-down wire pencil cup in one of the side chambers.

598 The other side had the same empty pencil cup. A test mouse was allowed 10 min to

599 investigate the three chambers. For social novelty session, another stranger mouse

600 (stranger2) was placed into the empty pencil cup and test mouse was allowed another 10

601 min to investigate between three chambers. The time mice spent in each chamber was

602 recorded and analyzed using BIOBSERVE III tracking system.

603

Data analysis

605 Experiments and data analyses were performed blindly by coding viruses. Unpaired t-test

606 or one-way ANOVA or two-way ANOVA or repeat measures ANOVA were used to analyze

607 slice physiology data or immunohistochemistry data or behavior data as indicated in figure

608 legends. Kolmogorov-Smirnov test was used to analyze the cumulative curves of mEPSCs

609 or mIPSCs. Significance was indicated as $*p < 0.05$, $**p < 0.01$, $***p < 0.001$. Data are

610 expressed as means ± SEM.

611

AUTHOR CONTRIBUTIONS

613 Z.L. performed AAV preparation, stereotactic injections, qRT-PCR, immunoblotting,

614 immunohistochemistry, biocytin morphological study, cerebellar electrophysiology and

615 behavior; M.J. designed sgRNAs, made the sgRNA vector and tested sgRNAs genome

616 editing efficiency; K.L.A. performed in-situ hybridization; J.K. provided antibodies against

617 Clstn1/2 and Clstn3, and R.S.Z. performed additional electrophysiological recordings. Z.L.,

618 M.J., and K.L.A. analyzed the data. Z.L. and T.C.S. wrote the manuscript.

619

625   **CONFLICT OF INTEREST**

626   The authors declare no conflict of interest.

REFERENCE

Anderson, G.R., S. Maxeiner, R. Sando, T. Tsetsenis, R.C. Malenka, and T.C. Sudhof. 2017. Postsynaptic adhesion GPCR latrophilin-2 mediates target recognition in entorhinal-hippocampal synapse assembly. *J Cell Biol*. 216:3831-3846. DOI: 10.1083/jcb.201703042, PMCID: 5674891

Araki, Y., T. Kawano, H. Taru, Y. Saito, S. Wada, K. Miyamoto, H. Kobayashi, H.O. Ishikawa, Y. Ohsugi, T. Yamamoto, K. Matsuno, M. Kinjo, and T. Suzuki. 2007. The novel cargo Alcadein induces vesicle association of kinesin-1 motor components and activates axonal transport. *EMBO J*. 26:1475-1486. DOI: 10.1038/sj.emboj.7601609, PMCID: 1829376

Araki, Y., S. Tomita, H. Yamaguchi, N. Miyagi, A. Sumioka, Y. Kirino, and T. Suzuki. 2003. Novel cadherin-related membrane proteins, Alcadeins, enhance the X11-like protein-mediated stabilization of amyloid beta-protein precursor metabolism. *J Biol Chem*. 278:49448-49458. DOI: 10.1074/jbc.M306024200, PMCID:

Attardo, A., J.E. Fitzgerald, and M.J. Schnitzer. 2015. Impermanence of dendritic spines in live adult CA1 hippocampus. *Nature*. 523:592-596. DOI: 10.1038/nature14467, PMCID: 4648621

Baude, A., E. Molnar, D. Latawiec, R.A. McIlhinney, and P. Somogyi. 1994. Synaptic and nonsynaptic localization of the GluR1 subunit of the AMPA-type excitatory amino acid receptor in the rat cerebellum. *J Neurosci*. 14:2830-2843. DOI: PMCID: 6577479

Bolliger, M.F., D.C. Martinelli, and T.C. Sudhof. 2011. The cell-adhesion G protein-coupled receptor BAI3 is a high-affinity receptor for C1q-like proteins. *Proc Natl Acad Sci U S A*. 108:2534-2539. DOI: 10.1073/pnas.1019577108, PMCID: 3038708

Briatore, F., G. Pregno, S. Di Angelantonio, E. Frola, M.E. De Stefano, C. Vaillend, M. Sassoe-Pognetto, and A. Patrizi. 2020. Dystroglycan Mediates Clustering of Essential GABAergic Components in Cerebellar Purkinje Cells. *Front Mol Neurosci*. 13:164. DOI: 10.3389/fnmol.2020.00164, PMCID: 7485281

Brinkman, E.K., T. Chen, M. Amendola, and B. van Steensel. 2014. Easy quantitative assessment of genome editing by sequence trace decomposition. *Nucleic Acids Res*. 42:e168. DOI: 10.1093/nar/gku936, PMCID: 4267669

Caillard, O., H. Moreno, B. Schwaller, I. Llano, M.R. Celio, and A. Marty. 2000. Role of the calcium-binding protein parvalbumin in short-term synaptic plasticity. *Proc Natl Acad Sci U S A*. 97:13372-13377. DOI: 10.1073/pnas.230362997, PMCID: 27231

Cesa, R., and P. Strata. 2009. Axonal competition in the synaptic wiring of the cerebellar cortex during development and in the mature cerebellum. *Neuroscience*. 162:624-632. DOI: 10.1016/j.neuroscience.2009.02.061, PMCID:

Chanda, S., W.D. Hale, B. Zhang, M. Wernig, and T.C. Sudhof. 2017. Unique versus Redundant Functions of Neuroligin Genes in Shaping Excitatory and Inhibitory

667   Synapse Properties. *J Neurosci*. 37:6816-6836. DOI:
668   10.1523/JNEUROSCI.0125-17.2017, PMCID: 5518416

669 Chen, L.Y., M. Jiang, B. Zhang, O. Gokce, and T.C. Sudhof. 2017. Conditional Deletion of
670   All Neurexins Defines Diversity of Essential Synaptic Organizer Functions for
671   Neurexins. *Neuron*. 94:611-625 e614. DOI: 10.1016/j.neuron.2017.04.011, PMCID:
672   5501922

673 Dickinson, M.E., A.M. Flenniken, X. Ji, L. Teboul, M.D. Wong, J.K. White, T.F. Meehan, W.J.
674   Weninger, H. Westerberg, H. Adissu, C.N. Baker, L. Bower, J.M. Brown, L.B. Caddle,
675   F. Chiani, D. Clary, J. Cleak, M.J. Daly, J.M. Denegre, B. Doe, M.E. Dolan, S.M.
676   Edie, H. Fuchs, V. Gailus-Durner, A. Galli, A. Gambadoro, J. Gallegos, S. Guo, N.R.
677   Horner, C.W. Hsu, S.J. Johnson, S. Kalaga, L.C. Keith, L. Lanoue, T.N. Lawson, M.
678   Lek, M. Mark, S. Marschall, J. Mason, M.L. McElwee, S. Newbigging, L.M. Nutter,
679   K.A. Peterson, R. Ramirez-Solis, D.J. Rowland, E. Ryder, K.E. Samocha, J.R.
680   Seavitt, M. Selloum, Z. Szoke-Kovacs, M. Tamura, A.G. Trainor, I. Tudose, S.
681   Wakana, J. Warren, O. Wendling, D.B. West, L. Wong, A. Yoshiki, C. International
682   Mouse Phenotyping, L. Jackson, I.C.d.l.S. Infrastructure Nationale Phenomin, L.
683   Charles River, M.R.C. Harwell, P. Toronto Centre for, I. Wellcome Trust Sanger, R.B.
684   Center, D.G. MacArthur, G.P. Tocchini-Valentini, X. Gao, P. Flicek, A. Bradley, W.C.
685   Skarnes, M.J. Justice, H.E. Parkinson, M. Moore, S. Wells, R.E. Braun, K.L.
686   Svenson, M.H. de Angelis, Y. Herault, T. Mohun, A.M. Mallon, R.M. Henkelman, S.D.
687   Brown, D.J. Adams, K.C. Lloyd, C. McKerlie, A.L. Beaudet, M. Bucan, and S.A.
688   Murray. 2016. High-throughput discovery of novel developmental phenotypes.
689   *Nature*. 537:508-514. DOI: 10.1038/nature19356, PMCID: 5295821

690 Dinamarca, M.C., A. Raveh, A. Schneider, T. Fritzius, S. Fruh, P.D. Rem, M. Stawarski, T.
691   Lalanne, R. Turecek, M. Choo, V. Besseyrias, W. Bildl, D. Bentrop, M. Staufenbiel,
692   M. Gassmann, B. Fakler, J. Schwenk, and B. Bettler. 2019. Complex formation of
693   APP with GABAB receptors links axonal trafficking to amyloidogenic processing. *Nat*
694   *Commun*. 10:1331. DOI: 10.1038/s41467-019-09164-3, PMCID: 6430795

695 Eccles, J.C., R. Llinas, and K. Sasaki. 1966. The excitatory synaptic action of climbing
696   fibres on the Purkinje cells of the cerebellum. *J Physiol*. 182:268-296. DOI:
697   10.1113/jphysiol.1966.sp007824, PMCID: 1357472

698 Emperador-Melero, J., G. de Nola, and P.S. Kaeser. 2021. Intact synapse structure and
699   function after combined knockout of PTPdelta, PTPsigma, and LAR. *Elife*. 10. DOI:
700   10.7554/eLife.66638, PMCID: 7963474

701 Foster, K.A., and W.G. Regehr. 2004. Variance-mean analysis in the presence of a rapid
702   antagonist indicates vesicle depletion underlies depression at the climbing fiber
703   synapse. *Neuron*. 43:119-131. DOI: 10.1016/j.neuron.2004.06.022, PMCID:

704 Fritschy, J.M., P. Panzanelli, J.E. Kralic, K.E. Vogt, and M. Sassoe-Pognetto. 2006.
705   Differential dependence of axo-dendritic and axo-somatic GABAergic synapses on
706   GABAA receptors containing the alpha1 subunit in Purkinje cells. *J Neurosci*.
707   26:3245-3255. DOI: 10.1523/JNEUROSCI.5118-05.2006, PMCID: 6674111

Fukai, S., and T. Yoshida. 2020. Roles of type IIa receptor protein tyrosine phosphatases as synaptic organizers. *FEBS J*. DOI: 10.1111/febs.15666, PMCID:

Gotoh, N., Y. Saito, S. Hata, H. Saito, D. Ojima, C. Murayama, M. Shigeta, T. Abe, D. Konno, F. Matsuzaki, T. Suzuki, and T. Yamamoto. 2020. Amyloidogenic processing of amyloid beta protein precursor (APP) is enhanced in the brains of alcadein alpha-deficient mice. *J Biol Chem*. 295:9650-9662. DOI: 10.1074/jbc.RA119.012386, PMCID: 7363152

Grimm, D., J.S. Lee, L. Wang, T. Desai, B. Akache, T.A. Storm, and M.A. Kay. 2008. In vitro and in vivo gene therapy vector evolution via multispecies interbreeding and retargeting of adeno-associated viruses. *J Virol*. 82:5887-5911. DOI: 10.1128/JVI.00254-08, PMCID: 2395137

Hintsch, G., A. Zurlinden, V. Meskenaite, M. Steuble, K. Fink-Widmer, J. Kinter, and P. Sonderegger. 2002. The calsyntenins--a family of postsynaptic membrane proteins with distinct neuronal expression patterns. *Mol Cell Neurosci*. 21:393-409. DOI: 10.1006/mcne.2002.1181, PMCID:

Hioki, H., F. Fujiyama, K. Taki, R. Tomioka, T. Furuta, N. Tamamaki, and T. Kaneko. 2003. Differential distribution of vesicular glutamate transporters in the rat cerebellar cortex. *Neuroscience*. 117:1-6. DOI: 10.1016/s0306-4522(02)00943-0, PMCID:

Incontro, S., C.S. Asensio, R.H. Edwards, and R.A. Nicoll. 2014. Efficient, complete deletion of synaptic proteins using CRISPR. *Neuron*. 83:1051-1057. DOI: 10.1016/j.neuron.2014.07.043, PMCID: 4195490

Kakegawa, W., N. Mitakidis, E. Miura, M. Abe, K. Matsuda, Y.H. Takeo, K. Kohda, J. Motohashi, A. Takahashi, S. Nagao, S. Muramatsu, M. Watanabe, K. Sakimura, A.R. Aricescu, and M. Yuzaki. 2015. Anterograde C1ql1 signaling is required in order to determine and maintain a single-winner climbing fiber in the mouse cerebellum. *Neuron*. 85:316-329. DOI: 10.1016/j.neuron.2014.12.020, PMCID:

Kim, H., D. Kim, J. Kim, H.Y. Lee, D. Park, H. Kang, K. Matsuda, F.H. Sterky, M. Yuzaki, J.Y. Kim, S.Y. Choi, J. Ko, and J.W. Um. 2020. Calsyntenin-3 interacts with both alpha- and beta-neurexins in the regulation of excitatory synaptic innervation in specific Schaffer collateral pathways. *J Biol Chem*. 295:9244-9262. DOI: 10.1074/jbc.RA120.013077, PMCID: 7335786

Ko, J., C. Zhang, D. Arac, A.A. Boucard, A.T. Brunger, and T.C. Sudhof. 2009. Neuroligin-1 performs neurexin-dependent and neurexin-independent functions in synapse validation. *EMBO J*. 28:3244-3255. DOI: 10.1038/emboj.2009.249, PMCID: 2771087

Konecna, A., R. Frischknecht, J. Kinter, A. Ludwig, M. Steuble, V. Meskenaite, M. Indermuhle, M. Engel, C. Cen, J.M. Mateos, P. Streit, and P. Sonderegger. 2006. Calsyntenin-1 docks vesicular cargo to kinesin-1. *Mol Biol Cell*. 17:3651-3663. DOI: 10.1091/mbc.e06-02-0112, PMCID: 1525238

Lipina, T.V., T. Prasad, D. Yokomaku, L. Luo, S.A. Connor, H. Kawabe, Y.T. Wang, N. Brose, J.C. Roder, and A.M. Craig. 2016. Cognitive Deficits in

749   Calsyntenin-2-deficient Mice Associated with Reduced GABAergic Transmission.
750   *Neuropsychopharmacology*. 41:802-810. DOI: 10.1038/npp.2015.206, PMCID:
751   4707826

752 Lisman, J.E., S. Raghavachari, and R.W. Tsien. 2007. The sequence of events that
753   underlie quantal transmission at central glutamatergic synapses. *Nat Rev Neurosci*.
754   8:597-609. DOI: 10.1038/nrn2191, PMCID:

755 Llano, I., A. Marty, C.M. Armstrong, and A. Konnerth. 1991. Synaptic- and agonist-induced
756   excitatory currents of Purkinje cells in rat cerebellar slices. *J Physiol*. 434:183-213.
757   DOI: 10.1113/jphysiol.1991.sp018465, PMCID: 1181413

758 Ludwig, A., J. Blume, T.M. Diep, J. Yuan, J.M. Mateos, K. Leuthauser, M. Steuble, P. Streit,
759   and P. Sonderegger. 2009. Calsyntenins mediate TGN exit of APP in a
760   kinesin-1-dependent manner. *Traffic*. 10:572-589. DOI:
761   10.1111/j.1600-0854.2009.00886.x, PMCID:

762 Meng, X., C.M. McGraw, W. Wang, J. Jing, S.Y. Yeh, L. Wang, J. Lopez, A.M. Brown, T.
763   Lin, W. Chen, M. Xue, R.V. Sillitoe, X. Jiang, and H.Y. Zoghbi. 2019. Neurexophilin4
764   is a selectively expressed alpha-neurexin ligand that modulates specific cerebellar
765   synapses and motor functions. *Elife*. 8. DOI: 10.7554/eLife.46773, PMCID: 6763262

766 Missler, M., W. Zhang, A. Rohlmann, G. Kattenstroth, R.E. Hammer, K. Gottmann, and T.C.
767   Sudhof. 2003. Alpha-neurexins couple Ca2+ channels to synaptic vesicle exocytosis.
768   *Nature*. 423:939-948. DOI: 10.1038/nature01755, PMCID:

769 Miyazaki, T., M. Yamasaki, K. Hashimoto, M. Yamazaki, M. Abe, H. Usui, M. Kano, K.
770   Sakimura, and M. Watanabe. 2012. Cav2.1 in cerebellar Purkinje cells regulates
771   competitive excitatory synaptic wiring, cell survival, and cerebellar biochemical
772   compartmentalization. *J Neurosci*. 32:1311-1328. DOI:
773   10.1523/JNEUROSCI.2755-11.2012, PMCID: 6796260

774 Monday, H.R., T.J. Younts, and P.E. Castillo. 2018. Long-Term Plasticity of
775   Neurotransmitter Release: Emerging Mechanisms and Contributions to Brain
776   Function and Disease. *Annu Rev Neurosci*. 41:299-322. DOI:
777   10.1146/annurev-neuro-080317-062155, PMCID: 6238218

778 Nakayama, H., T. Miyazaki, K. Kitamura, K. Hashimoto, Y. Yanagawa, K. Obata, K.
779   Sakimura, M. Watanabe, and M. Kano. 2012. GABAergic inhibition regulates
780   developmental synapse elimination in the cerebellum. *Neuron*. 74:384-396. DOI:
781   10.1016/j.neuron.2012.02.032, PMCID:

782 Nelson, S.B., and V. Valakh. 2015. Excitatory/Inhibitory Balance and Circuit Homeostasis in
783   Autism Spectrum Disorders. *Neuron*. 87:684-698. DOI:
784   10.1016/j.neuron.2015.07.033, PMCID: 4567857

785 Ohno, H., S. Kato, Y. Naito, H. Kunitomo, M. Tomioka, and Y. Iino. 2014. Role of synaptic
786   phosphatidylinositol 3-kinase in a behavioral learning response in C. elegans.
787   *Science*. 345:313-317. DOI: 10.1126/science.1250709, PMCID:

788 Peng, J., A.L. Sheng, Q. Xiao, L. Shen, X.C. Ju, M. Zhang, S.T. He, C. Wu, and Z.G. Luo.
789   2019. Single-cell transcriptomes reveal molecular specializations of neuronal cell

790   types in the developing cerebellum. *J Mol Cell Biol*. 11:636-648. DOI:
791   10.1093/jmcb/mjy089, PMCID: 6788728

792 Pettem, K.L., D. Yokomaku, L. Luo, M.W. Linhoff, T. Prasad, S.A. Connor, T.J. Siddiqui, H.
793   Kawabe, F. Chen, L. Zhang, G. Rudenko, Y.T. Wang, N. Brose, and A.M. Craig.
794   2013. The specific alpha-neurexin interactor calsyntenin-3 promotes excitatory and
795   inhibitory synapse development. *Neuron*. 80:113-128. DOI:
796   10.1016/j.neuron.2013.07.016, PMCID: 3821696

797 Pfeiffer, T., S. Poll, S. Bancelin, J. Angibaud, V.K. Inavalli, K. Keppler, M. Mittag, M.
798   Fuhrmann, and U.V. Nagerl. 2018. Chronic 2P-STED imaging reveals high turnover
799   of dendritic spines in the hippocampus in vivo. *Elife*. 7. DOI: 10.7554/eLife.34700,
800   PMCID: 6014725

801 Platt, R.J., S. Chen, Y. Zhou, M.J. Yim, L. Swiech, H.R. Kempton, J.E. Dahlman, O. Parnas,
802   T.M. Eisenhaure, M. Jovanovic, D.B. Graham, S. Jhunjhunwala, M. Heidenreich, R.J.
803   Xavier, R. Langer, D.G. Anderson, N. Hacohen, A. Regev, G. Feng, P.A. Sharp, and
804   F. Zhang. 2014. CRISPR-Cas9 knockin mice for genome editing and cancer
805   modeling. *Cell*. 159:440-455. DOI: 10.1016/j.cell.2014.09.014, PMCID: 4265475

806 Ranneva, S.V., V.F. Maksimov, I.M. Korostyshevskaja, and T.V. Lipina. 2020. Lack of
807   synaptic protein, calsyntenin-2, impairs morphology of synaptic complexes in mice.
808   *Synapse*. 74:e22132. DOI: 10.1002/syn.22132, PMCID:

809 Südhof, T.C. 2021. The Cell Biology of Synapse Formation. *Journal of Cell Biology*. in press.
810   DOI: PMCID:

811 Sando, R., X. Jiang, and T.C. Sudhof. 2019. Latrophilin GPCRs direct synapse specificity
812   by coincident binding of FLRTs and teneurins. *Science*. 363. DOI:
813   10.1126/science.aav7969, PMCID: 6636343

814 Sando, R., and T.C. Sudhof. 2021. Latrophilin GPCR signaling mediates synapse formation.
815   *Elife*. 10. DOI: 10.7554/eLife.65717, PMCID: 7954527

816 Saunders, A., E.Z. Macosko, A. Wysoker, M. Goldman, F.M. Krienen, H. de Rivera, E. Bien,
817   M. Baum, L. Bortolin, S. Wang, A. Goeva, J. Nemesh, N. Kamitaki, S. Brumbaugh, D.
818   Kulp, and S.A. McCarroll. 2018. Molecular Diversity and Specializations among the
819   Cells of the Adult Mouse Brain. *Cell*. 174:1015-1030 e1016. DOI:
820   10.1016/j.cell.2018.07.028, PMCID: 6447408

821 Schaum, N., J. Karkanias, N.F. Neff, A.P. May, S.R. Quake, T. Wyss-Coray, S. Darmanis, J.
822   Batson, O. Botvinnik, M.B. Chen, S. Chen, F. Green, R.C. Jones, A. Maynard, L.
823   Penland, A.O. Pisco, R.V. Sit, G.M. Stanley, J.T. Webber, F. Zanini, A.S. Baghel, I.
824   Bakerman, I. Bansal, D. Berdnik, B. Bilen, D. Brownfield, C. Cain, M.B. Chen, S.
825   Chen, M. Cho, G. Cirolia, S.D. Conley, S. Darmanis, A. Demers, K. Demir, A. de
826   Morree, T. Divita, H. du Bois, L.B.T. Dulgeroff, H. Ebadi, F.H. Espinoza, M. Fish, Q.
827   Gan, B.M. George, A. Gillich, F. Green, G. Genetiano, X. Gu, G.S. Gulati, Y. Hang, S.
828   Hosseinzadeh, A. Huang, T. Iram, T. Isobe, F. Ives, R.C. Jones, K.S. Kao, G.
829   Karnam, A.M. Kershner, B.M. Kiss, W. Kong, M.E. Kumar, J.Y. Lam, D.P. Lee, S.E.
830   Lee, G. Li, Q. Li, L. Liu, A. Lo, W.-J. Lu, A. Manjunath, A.P. May, K.L. May, O.L. May,

831   A. Maynard, M. McKay, R.J. Metzger, M. Mignardi, D. Min, A.N. Nabhan, N.F. Neff,
832   K.M. Ng, J. Noh, R. Patkar, W.C. Peng, L. Penland, R. Puccinelli, E.J. Rulifson, N.
833   Schaum, S.S. Sikandar, R. Sinha, R.V. Sit, K. Szade, W. Tan, C. Tato, K. Tellez, K.J.
834   Travaglini, C. Tropini, L. Waldburger, L.J. van Weele, et al. 2018. Single-cell
835   transcriptomics of 20 mouse organs creates a Tabula Muris. *Nature*. 562:367-372.
836   DOI: 10.1038/s41586-018-0590-4, PMCID:

837 Schwenk, J., E. Perez-Garci, A. Schneider, A. Kollewe, A. Gauthier-Kemper, T. Fritzius, A.
838   Raveh, M.C. Dinamarca, A. Hanuschkin, W. Bildl, J. Klingauf, M. Gassmann, U.
839   Schulte, B. Bettler, and B. Fakler. 2016. Modular composition and dynamics of
840   native GABAB receptors identified by high-resolution proteomics. *Nat Neurosci*.
841   19:233-242. DOI: 10.1038/nn.4198, PMCID:

842 Sclip, A., and T.C. Sudhof. 2020. LAR receptor phospho-tyrosine phosphatases regulate
843   NMDA-receptor responses. *Elife*. 9. DOI: 10.7554/eLife.53406, PMCID: 6984820

844 Sigoillot, S.M., K. Iyer, F. Binda, I. Gonzalez-Calvo, M. Talleur, G. Vodjdani, P. Isope, and F.
845   Selimi. 2015. The Secreted Protein C1QL1 and Its Receptor BAI3 Control the
846   Synaptic Connectivity of Excitatory Inputs Converging on Cerebellar Purkinje Cells.
847   *Cell Rep*. 10:820-832. DOI: 10.1016/j.celrep.2015.01.034, PMCID:

848 Sotelo, C. 1975. Anatomical, physiological and biochemical studies of the cerebellum from
849   mutant mice. II. Morphological study of cerebellar cortical neurons and circuits in the
850   weaver mouse. *Brain Res*. 94:19-44. DOI: 10.1016/0006-8993(75)90874-4, PMCID:

851 Ster, J., M. Steuble, C. Orlando, T.M. Diep, A. Akhmedov, O. Raineteau, V. Pernet, P.
852   Sonderegger, and U. Gerber. 2014. Calsyntenin-1 regulates targeting of dendritic
853   NMDA receptors and dendritic spine maturation in CA1 hippocampal pyramidal cells
854   during postnatal development. *J Neurosci*. 34:8716-8727. DOI:
855   10.1523/JNEUROSCI.0144-14.2014, PMCID: 6608200

856 Strata, P., F. Tempia, M. Zagrebelsky, and F. Rossi. 1997. Reciprocal trophic interactions
857   between climbing fibres and Purkinje cells in the rat cerebellum. *Prog Brain Res*.
858   114:263-282. DOI: 10.1016/s0079-6123(08)63369-5, PMCID:

859 Tasic, B., Z. Yao, L.T. Graybuck, K.A. Smith, T.N. Nguyen, D. Bertagnolli, J. Goldy, E.
860   Garren, M.N. Economo, S. Viswanathan, O. Penn, T. Bakken, V. Menon, J. Miller, O.
861   Fong, K.E. Hirokawa, K. Lathia, C. Rimorin, M. Tieu, R. Larsen, T. Casper, E.
862   Barkan, M. Kroll, S. Parry, N.V. Shapovalova, D. Hirschstein, J. Pendergraft, H.A.
863   Sullivan, T.K. Kim, A. Szafer, N. Dee, P. Groblewski, I. Wickersham, A. Cetin, J.A.
864   Harris, B.P. Levi, S.M. Sunkin, L. Madisen, T.L. Daigle, L. Looger, A. Bernard, J.
865   Phillips, E. Lein, M. Hawrylycz, K. Svoboda, A.R. Jones, C. Koch, and H. Zeng. 2018.
866   Shared and distinct transcriptomic cell types across neocortical areas. *Nature*.
867   563:72-78. DOI: 10.1038/s41586-018-0654-5, PMCID: 6456269

868 Vagnoni, A., M.S. Perkinton, E.H. Gray, P.T. Francis, W. Noble, and C.C. Miller. 2012.
869   Calsyntenin-1 mediates axonal transport of the amyloid precursor protein and
870   regulates Abeta production. *Hum Mol Genet*. 21:2845-2854. DOI:
871   10.1093/hmg/dds109, PMCID: 3373235

872 Vogt, L., S.P. Schrimpf, V. Meskenaite, R. Frischknecht, J. Kinter, D.P. Leone, U. Ziegler,
873   and P. Sonderegger. 2001. Calsyntenin-1, a proteolytically processed postsynaptic
874   membrane protein with a cytoplasmic calcium-binding domain. *Mol Cell Neurosci*.
875   17:151-166. DOI: 10.1006/mcne.2000.0937, PMCID:
876 Wang, C.Y., Z. Liu, Y.H. Ng, and T.C. Sudhof. 2020. A Synaptic Circuit Required for
877   Acquisition but Not Recall of Social Transmission of Food Preference. *Neuron*.
878   107:144-157 e144. DOI: 10.1016/j.neuron.2020.04.004, PMCID: 7351611
879 Wu, X., W.K. Morishita, A.M. Riley, W.D. Hale, T.C. Sudhof, and R.C. Malenka. 2019.
880   Neuroligin-1 Signaling Controls LTP and NMDA Receptors by Distinct Molecular
881   Pathways. *Neuron*. 102:621-635 e623. DOI: 10.1016/j.neuron.2019.02.013, PMCID:
882   6509009
883 Yamasaki, M., K. Hashimoto, and M. Kano. 2006. Miniature synaptic events elicited by
884   presynaptic Ca2+ rise are selectively suppressed by cannabinoid receptor activation
885   in cerebellar Purkinje cells. *J Neurosci*. 26:86-95. DOI:
886   10.1523/JNEUROSCI.2258-05.2006, PMCID: 6674295
887 Yuzaki, M., and A.R. Aricescu. 2017. A GluD Coming-Of-Age Story. *Trends Neurosci*.
888   40:138-150. DOI: 10.1016/j.tins.2016.12.004, PMCID: 5553105
889 Zeisel, A., H. Hochgerner, P. Lonnerberg, A. Johnsson, F. Memic, J. van der Zwan, M.
890   Haring, E. Braun, L.E. Borm, G. La Manno, S. Codeluppi, A. Furlan, K. Lee, N.
891   Skene, K.D. Harris, J. Hjerling-Leffler, E. Arenas, P. Ernfors, U. Marklund, and S.
892   Linnarsson. 2018. Molecular Architecture of the Mouse Nervous System. *Cell*.
893   174:999-1014 e1022. DOI: 10.1016/j.cell.2018.06.021, PMCID: 6086934
894 Zeng, X., M. Ye, J.M. Resch, M.P. Jedrychowski, B. Hu, B.B. Lowell, D.D. Ginty, and B.M.
895   Spiegelman. 2019. Innervation of thermogenic adipose tissue via a calsyntenin
896   3beta-S100b axis. *Nature*. 569:229-235. DOI: 10.1038/s41586-019-1156-9, PMCID:
897   6589139
898 Zhang, B., L.Y. Chen, X. Liu, S. Maxeiner, S.J. Lee, O. Gokce, and T.C. Sudhof. 2015.
899   Neuroligins Sculpt Cerebellar Purkinje-Cell Circuits by Differential Control of Distinct
900   Classes of Synapses. *Neuron*. 87:781-796. DOI: 10.1016/j.neuron.2015.07.020,
901   PMCID: 4545494
902 Zhou, M., M.D. Melin, W. Xu, and T.C. Sudhof. 2020. Dysfunction of parvalbumin neurons
903   in the cerebellar nuclei produces an action tremor. *J Clin Invest*. 130:5142-5156. DOI:
904   10.1172/JCI135802, PMCID: 7524475

FIGURES and FIGURE LEGENDS

906
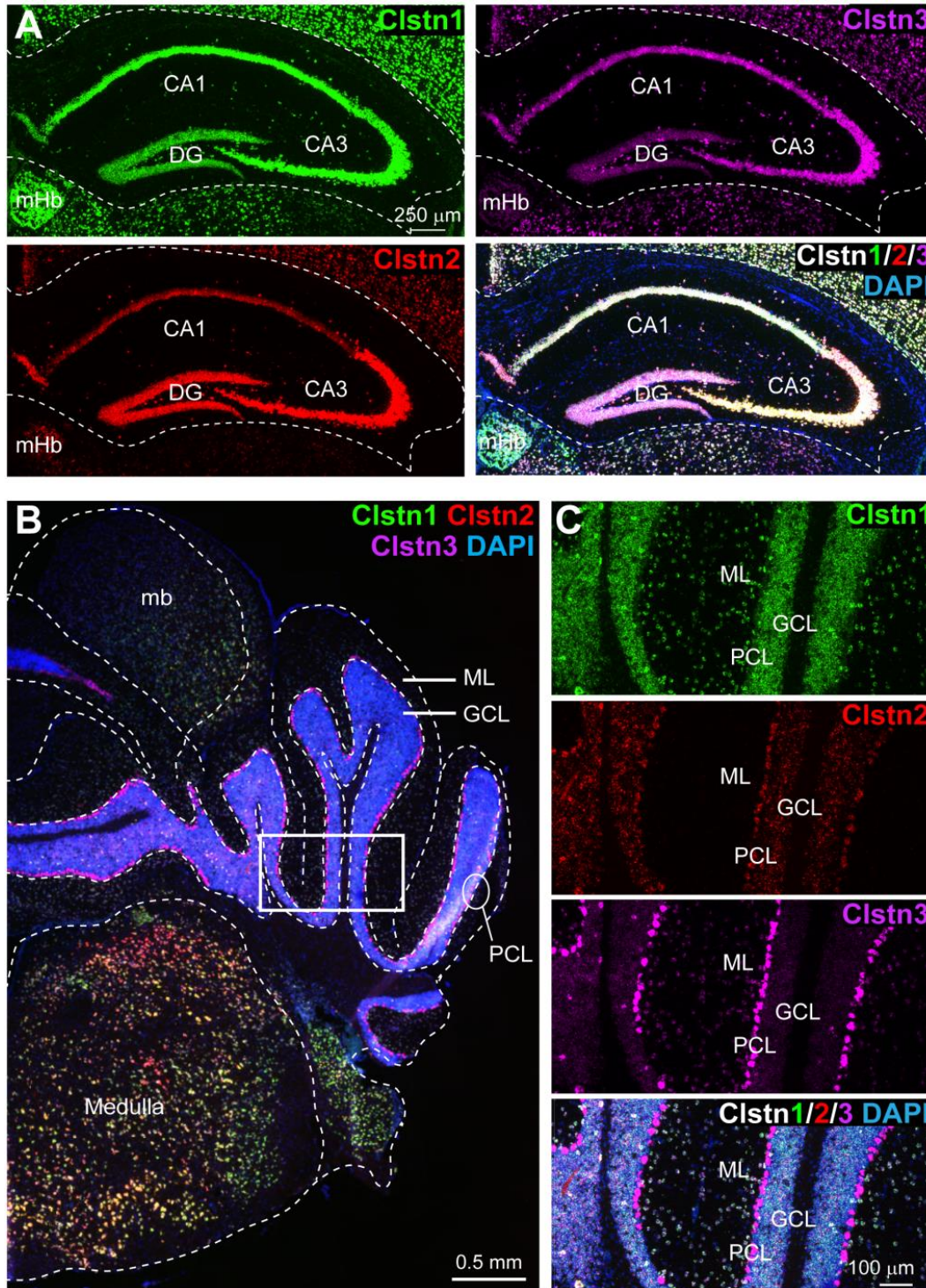
Figure 1: *Clstn1*, *Clstn2*, and *Clstn3* expression targets overlapping neuronal populations in the dorsal hippocampus, but distinct neuronal populations in the cerebellum of mice

(A) *Clstn1* (green), *Clstn2* (red) and *Clstn3* (magenta) exhibit distinct but largely overlapping expression patterns in the dorsal hippocampus. Representative images show sections from a mouse at P30 labeled by single-molecule *in situ* fluorescent hybridization

913 (RNAscope) and by DAPI staining as indicated (DG, dentate gyrus; CA1 and CA3, CA1-
914 and CA3-regions of the hippocampus proper; mHb, medial habenula).

915 **(B & C)** *Clstn1* (green), *Clstn2* (red) and *Clstn3* (magenta) are expressed in separate and
916 largely non-overlapping patterns in the cerebellum as visualized by single-molecule *in situ*
917 hybridization (B, overview; C, expanded views of the area boxed in B; Mb, midbrain; ML,
918 molecular layer; PCL, Purkinje cell layer; GCL, granule cell layer). Scale bars apply to all
919 images in a set.

920
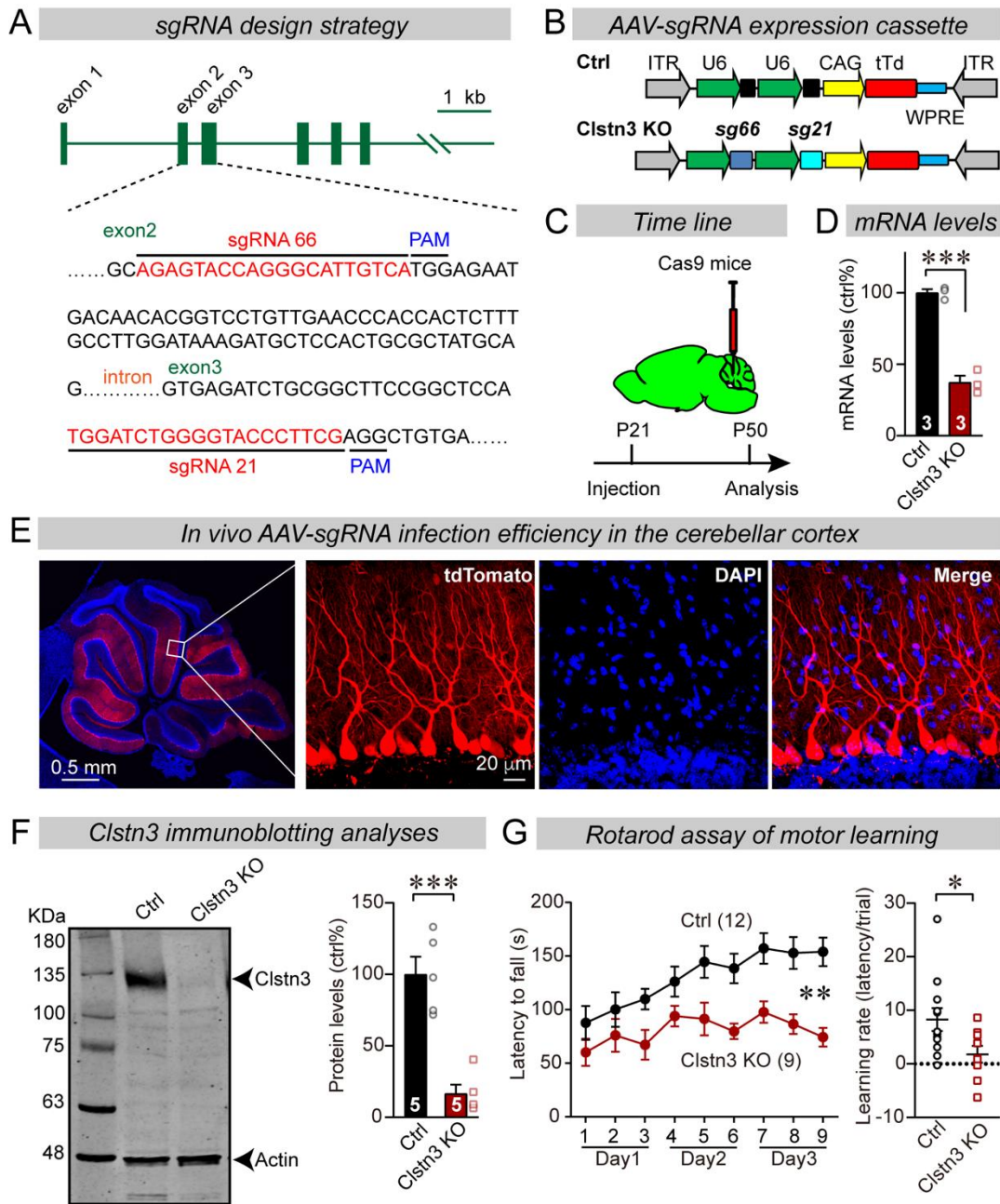
Figure 2: CRISPR/Cas9 manipulations enable rapid and highly efficient *in vivo* deletions of *Clstn3* in Purkinje cells, resulting in a severe impairment in motor learning

(A) Schematic of the sgRNA design strategy. Both sgRNAs target the positive strand of DNA, with sg66 targeting exon2, and sg21 targeting exon3.

(B) Schematic of the AAV-DJ expression cassette in which sgRNAs and tdTomato (tdT) synthesis are driven by U6 and CAG promoters, respectively. Control mice were infected with AAVs that lacked sgRNAs but were otherwise identical.

(C) Experimental strategy for CRISPR-mediated acute *Clstn3* deletions in the cerebellum. AAVs expressing the sgRNAs and tdTomato were stereotactically injected into the

35

932 cerebellum of constitutively expressing Cas9 mice at P21, and mice were analyzed after
933 P50.

934 **(D)** Quantitative RT-PCR shows that the CRISPR-mediated *Clstn3* deletion severely
935 suppresses *Clstn3* mRNA levels in the total cerebellum. Relative gene expression levels
936 were first normalized to GAPDH using threshold cycle (CT) values, and then normalized to
937 control.

938 **(E)** Representative images of a cerebellar section from a mouse that was stereotactically
939 infected with AAVs as described in **C** (left, overview of the cerebellum; right, cerebellar
940 cortex; red = AAV-encoded tdTomato; blue, DAPI). Note that AAVs infect all Purkinje cells
941 but few granule cells.

942 **(F)** Immunoblotting analyses confirm that the CRISPR-mediated deletion greatly
943 suppresses *Clstn3* protein levels (left, representative immunoblot; right, summary graph of
944 quantifications using fluorescently labeled secondary antibodies).

945 **(G)** The CRISPR-mediated *Clstn3* KO in cerebellar Purkinje cells severely impairs motor
946 learning as analyzed by the rotarod assay (left, rotarod curve; right, slope of rotarod curve
947 used as an index of the learning rate).

948 Data in panels D, F, and G are means ± SEM. Statistical analyses were performed using
949 unpaired t-test for D, F, and learning rate in G (*p<0.05, ***p<0.001) and repeat measures
950 ANOVA for rotarod curve in G ($F_{(1,19)}$=11.791, **p<0.01). Numbers of animals for each
951 experiment are indicated in graphs.
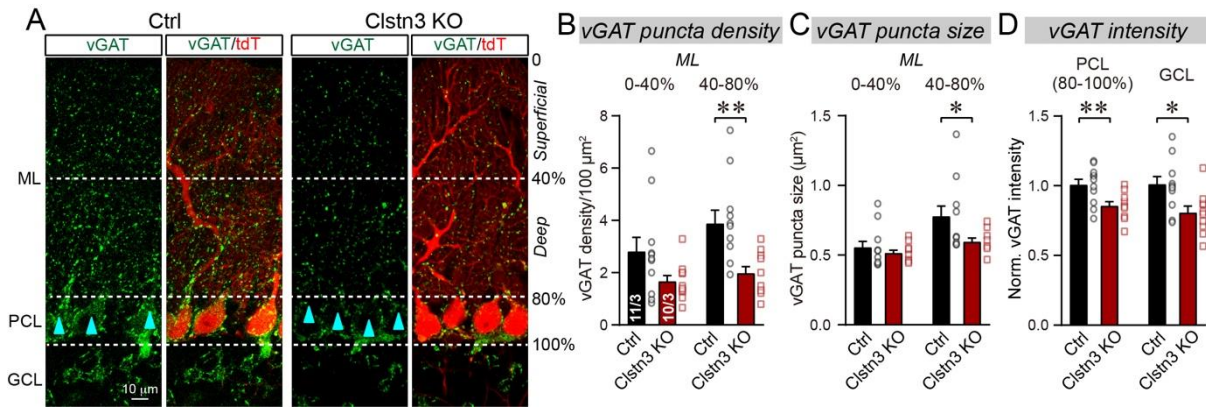
Figure 3: The *Clstn3* KO decreases inhibitory synapse numbers in the cerebellar cortex

(A) Representative confocal images of cerebellar cortex sections stained for vGAT and tdTomato. Sections are from mice in which Purkinje cells were infected with control AAVs (Ctrl) or AAVs that induce the CRISPR-mediated *Clstn3* KO (red, AAV-encoded tdTomato signal; green, vGAT; ML, molecular layer; PCL, Purkinje cell layer; GCL, granule cell layer). Calibration bar applies to all images.

(B-D) The Clstn3 KO in Purkinje cells suppresses the number of vGAT-positive synapses in the cerebellar cortex. Summary graphs show quantifications of the density (B) and size (C) of vGAT-positive puncta in the molecular layer (ML) of the cerebellar cortex (separated into deep and superficial areas), and of the vGAT-staining intensity in the Purkinje cell layer (PCL) and granule cell layer (GCL) of the cerebellar cortex (D). Data are means ± SEM (numbers of sections/mice analyzed are indicated in bar graphs). Statistical analyses were performed using unpaired t-tests, with *p<0.05, **p<0.01.
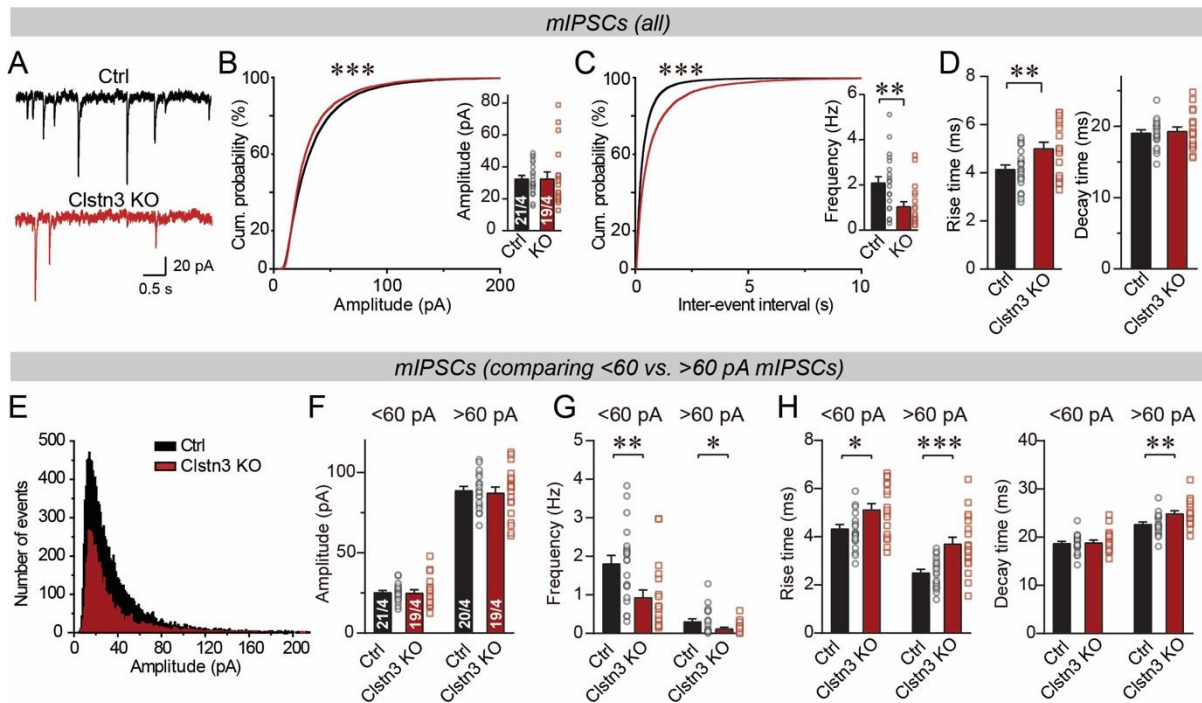
Figure 4: The *Clstn3* KO decreases spontaneous inhibitory synaptic 'mini' events in Purkinje cells

(A-C) The *Clstn3* KO decreases the frequency but not the amplitude of mIPSCs (A, representative traces; B, cumulative probability plot of the mIPSC amplitude [inset, average amplitude]; C, cumulative probability plot of the mIPSC inter-event interval [inset, average frequency]).

(D) The Purkinje cell *Clstn3* KO increases the rise but not decay time of mIPSCs.

(E) Plot of the number of mIPSC events vs. amplitude using a normal distribution.

(F-H) The *Clstn3* KO similarly impairs mIPSCs with a larger (>60 pA) and a smaller amplitude (<60 pA), which in Purkinje cells are likely generated primarily by basket-cell and stellate-cell synapses, respectively (F & G, summary graphs for the mIPSC amplitude (F) and frequency (G) separately analyzed for high- and low-amplitude events; H, mIPSC rise [left] and decay times [right], separately analyzed for high- and low-amplitude events).

All summary data are means ± SEM. Numbers of cells/mice analyzed are indicated in bar graphs. Statistical analyses were performed using unpaired t-tests (bar graphs with two groups) or Kolmogorov-Smirnov test (cumulative analysis), with *$p<0.05$, **$p<0.01$, ***$p<0.001$.

985
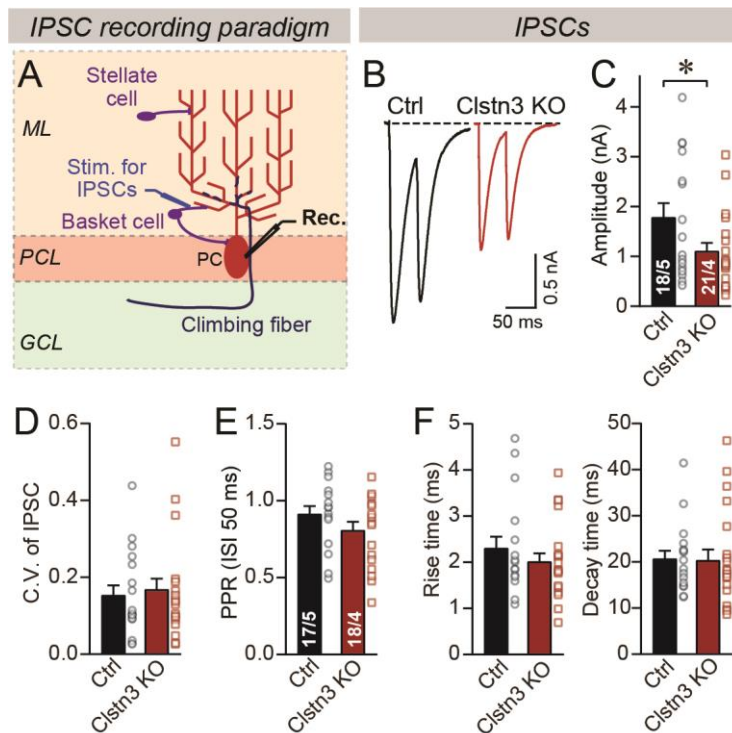
Figure 5: The *Clstn3* KO decreases evoked inhibitory synaptic responses in Purkinje cells

(A) Experimental design for recordings of IPSCs evoked by stimulation of basket cell axons (ML, molecular layer; PCL, Purkinje cell layer; GCL, granule cell layer; PC, Purkinje cell; Rec., recording patch pipette).

(B & C) The *Clstn3* KO decreases the amplitude of evoked basket-cell IPSCs (B, representative traces of pairs of evoked IPSCs with a 50 ms inter-stimulus interval; C, summary graphs of the amplitude of the first IPSC).

(D & E) The *Clstn3* KO in Purkinje cells does not affect the release probability at inhibitory synapses as judged by the coefficient of variation (D) and the paired-pulse ratio with an interstimulus interval of 50 ms (E) of evoked IPSCs.

(F) The *Clstn3* KO in Purkinje cells has no significant effect on IPSC kinetics (left, rise times; right, decay times of evoked ISPCs).

All summary data are means ± SEM. Numbers of cells/mice analyzed are indicated in bar graphs. Statistical analyses were performed using unpaired t-tests, with *p<0.05.
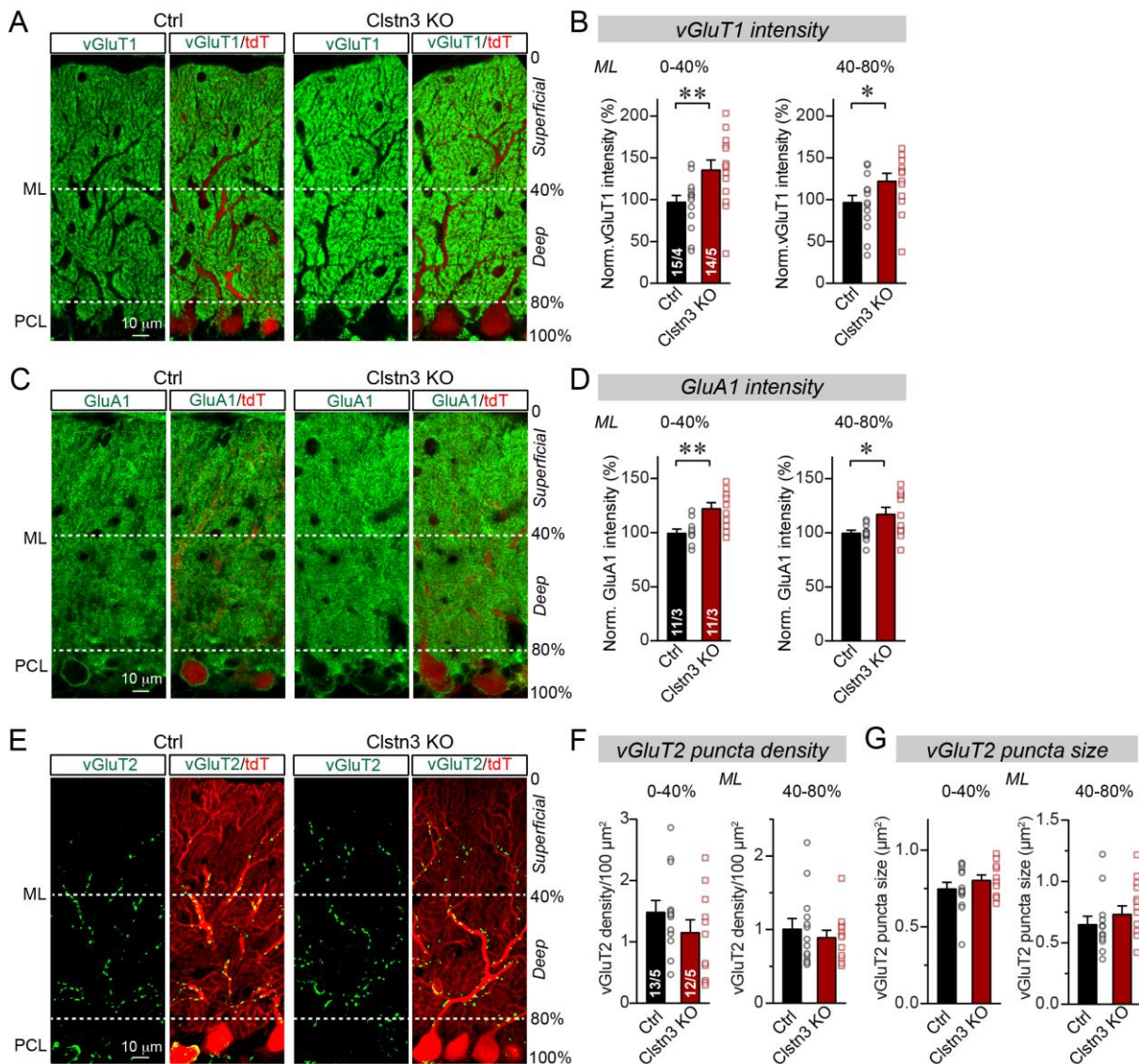
Figure 6: CRISPR-mediated *Clstn3* deletion in the cerebellar Purkinje cells increases parallel-fiber excitatory synapse numbers without changing climbing-fiber synapse numbers

(A & B) Immunostaining of cerebellar cortex sections with antibodies to vGluT1 as a presynaptic marker for parallel-fiber synapses reveals a significant increase (A, representative confocal images from control and *Clstn3* KO mice [green vGluT1; red, tdTomato]; B, summary graphs of the vGluT1 staining intensity in the superficial (0-40%) and deep (40-80%) molecular layers of the cerebellar cortex).

(**C & D**) Immunostaining with antibodies to GluA1, an astroglial marker for tripartite parallel-fiber/Bergmann glia synapses, also uncovers a significant increase in staining intensity (C, representative confocal images from control and *Clstn3* KO samples [green vGluT1; red, tdTomato]; D, summary graphs of the GluA1 staining intensity in the superficial (0-40%) and deep (40-80%) molecular layers of the cerebellar cortex).

(E-G) Immunostaining for vGluT2 as a marker for climbing-fiber synapses in cerebellar cortex fails to uncover a *Clstn3* KO-induced change (E, representative confocal images

40

1017 [green, vGluT2; red, tdTomato]; F & G, summary graphs of the density (F) and size (G) of
1018 vGluT2-positive synaptic puncta in the superficial (0-40%) and deep (40-80%) molecular
1019 layers of the cerebellar cortex).

1020 All numerical data are means ± SEM; numbers of sections/mice analyzed are indicated in
1021 the first bar graphs for each experiment. Statistical significance was assessed by unpaired
1022 Student's t-test (*$p<0.05$, **$p<0.01$).
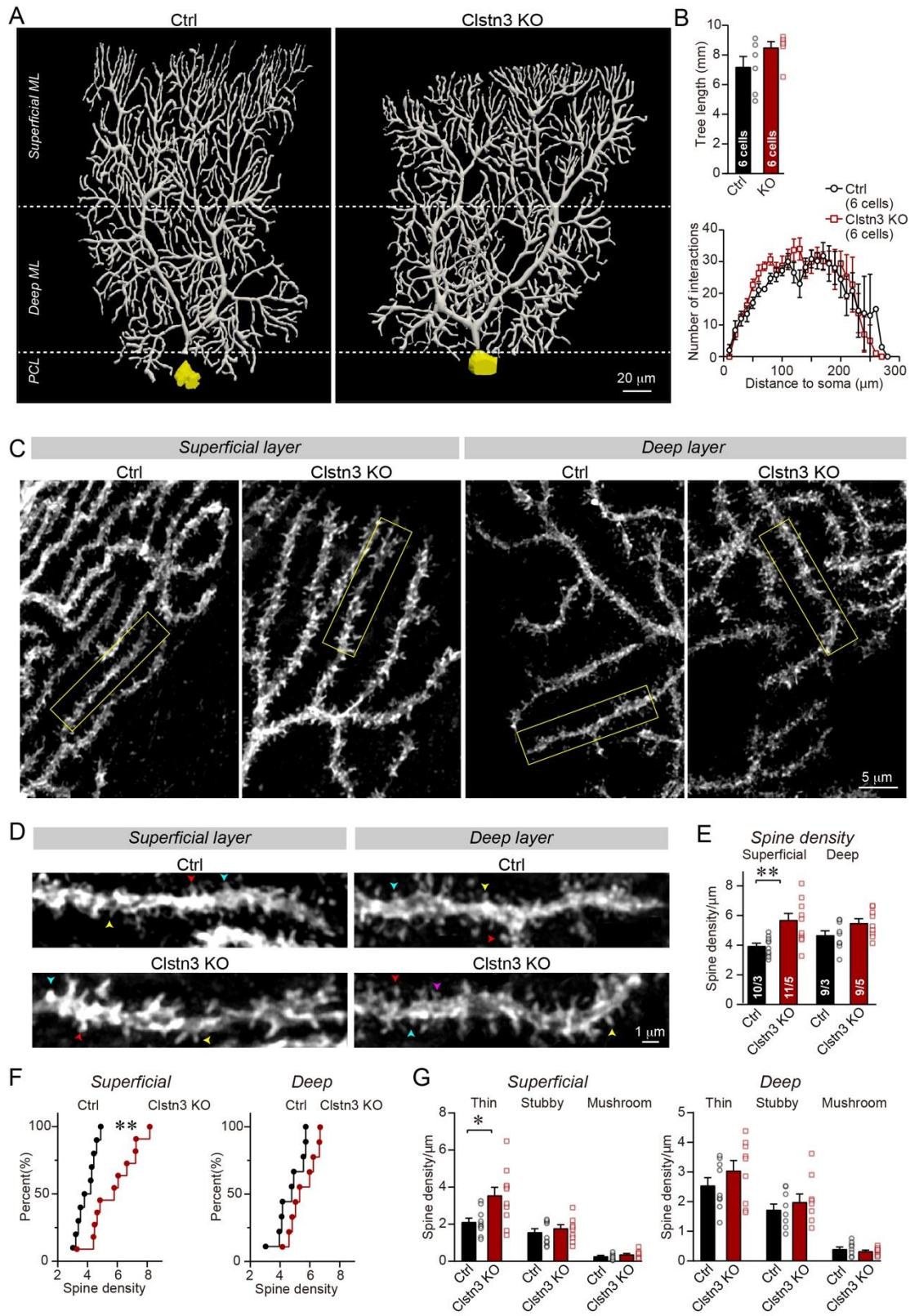
Figure 7: Morphological analysis of individual Purkinje cells reveals that the *Clstn3* KO robustly increases their dendritic spine density without significantly altering their dendritic arborization

(A & B) Biocytin filling of individual Purkinje cells via a patch pipette demonstrates that the *Clstn3* KO does not significantly change the overall dendritic architecture of Purkinje cells (A, representative images of Purkinje cell dendritic trees for control and *Clstn3* KO mice after 3D reconstruction [for more images, see Supplementary Fig. S6]; B, quantifications of the dendritic tree length [top] or dendritic arborization using Sholl analysis [bottom]).

(**C-F**) The *Clstn3* KO increases the density of dendritic spines of Purkinje cells in the superficial part of the cerebellar cortex (C & D, representative images of spiny dendrites at low and high magnifications, respectively; [blue, red, and yellows arrowheads mark different spine types]; E & F, summary graph [E] and cumulative distribution of the spine density [F]).

(G) The *Clstn3* KO in Purkinje cells increases preferentially the density of thin spines in the superficial part of the cerebellar cortex, based on a morphological classification of spine types into thin, stubby and mushroom spines.

All data in B, E, and G are means ± SEM; 6 control and Clstn3 KO Purkinje cells were reconstructed for B; numbers in the first bars of E indicate the number of cell/animal analyzed for E-G. Statistical significance (*p<0.05; **p<0.01) in B and G was assessed by an unpaired t-test, and in E by one-way ANOVA ($F_{(3, 35)}$=5.693, p=0.003), followed by Tukey's post hoc comparisons for control and *Clstn3* KO groups.
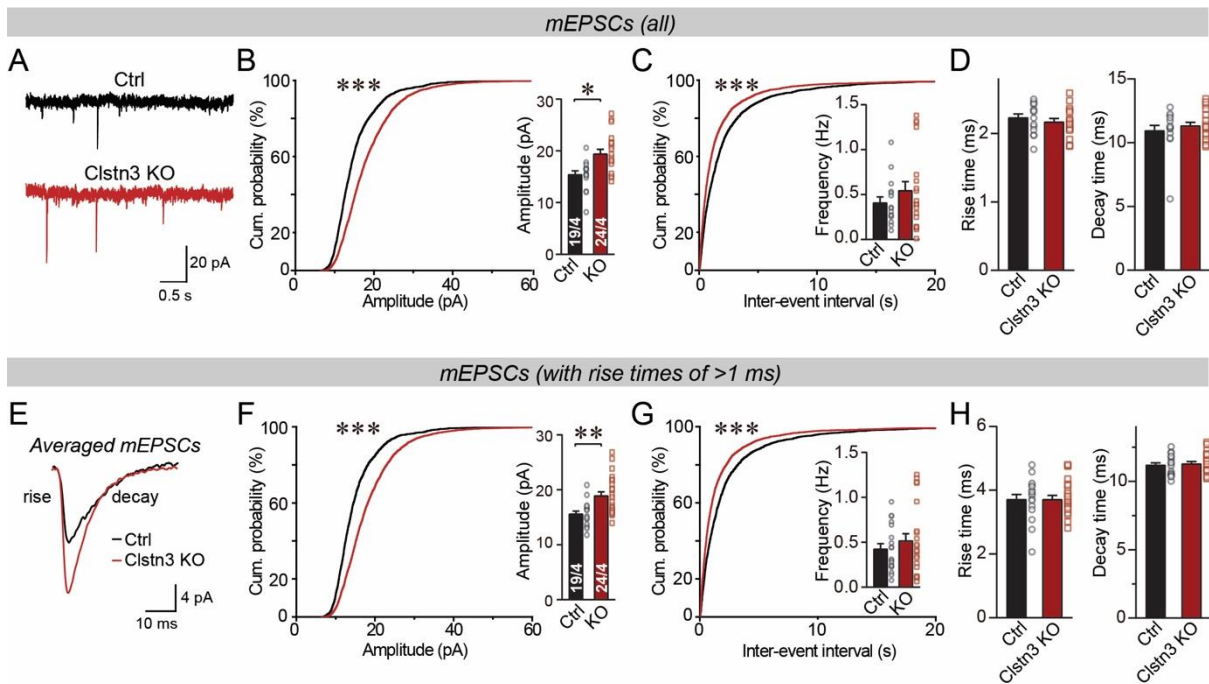
Figure 8: The *Clstn3* KO in cerebellar Purkinje cells increases the amplitude and frequency of parallel-fiber mEPSCs

(A-C) The *Clstn3* KO increases the amplitude and frequency of mEPSCs in Purkinje cells (A, representative traces; B, cumulative probability plot of the mEPSC amplitude [inset, average amplitude]; C, cumulative probability plot of the mEPSC inter-event interval [inset, average frequency]).

(D) The *Clstn3* KO in Purkinje cells has no effect on mEPSC kinetics (left, mEPSC rise times; right, mEPSC decay times).

(E) Expanded trace of averaged mEPSCs to illustrate the kinetic similarity of control and *Clstn3* KO events with a change in amplitude.

(F & G) mEPSCs with slow rise times (>1 ms) and that are likely exclusively derived from parallel-fiber synapses exhibit the same phenotype as the total mEPSCs (same as B & C, but for mEPSCs with slow rise times).

(H) The *Clstn3* KO in Purkinje cells has no effect on the kinetics of mEPSCs with slow rise times (left, mEPSC rise times; right, mEPSC decay times).

All numerical data are means ± SEM. Statistical significance with two groups was assessed by unpaired t-test (*p<0.05, **p<0.01), with the number of cells/mice analyzed indicated in the first bar graphs for each experiment. Cumulative analysis was done with Kolmogorov-Smirnov test (***p<0.001).

44
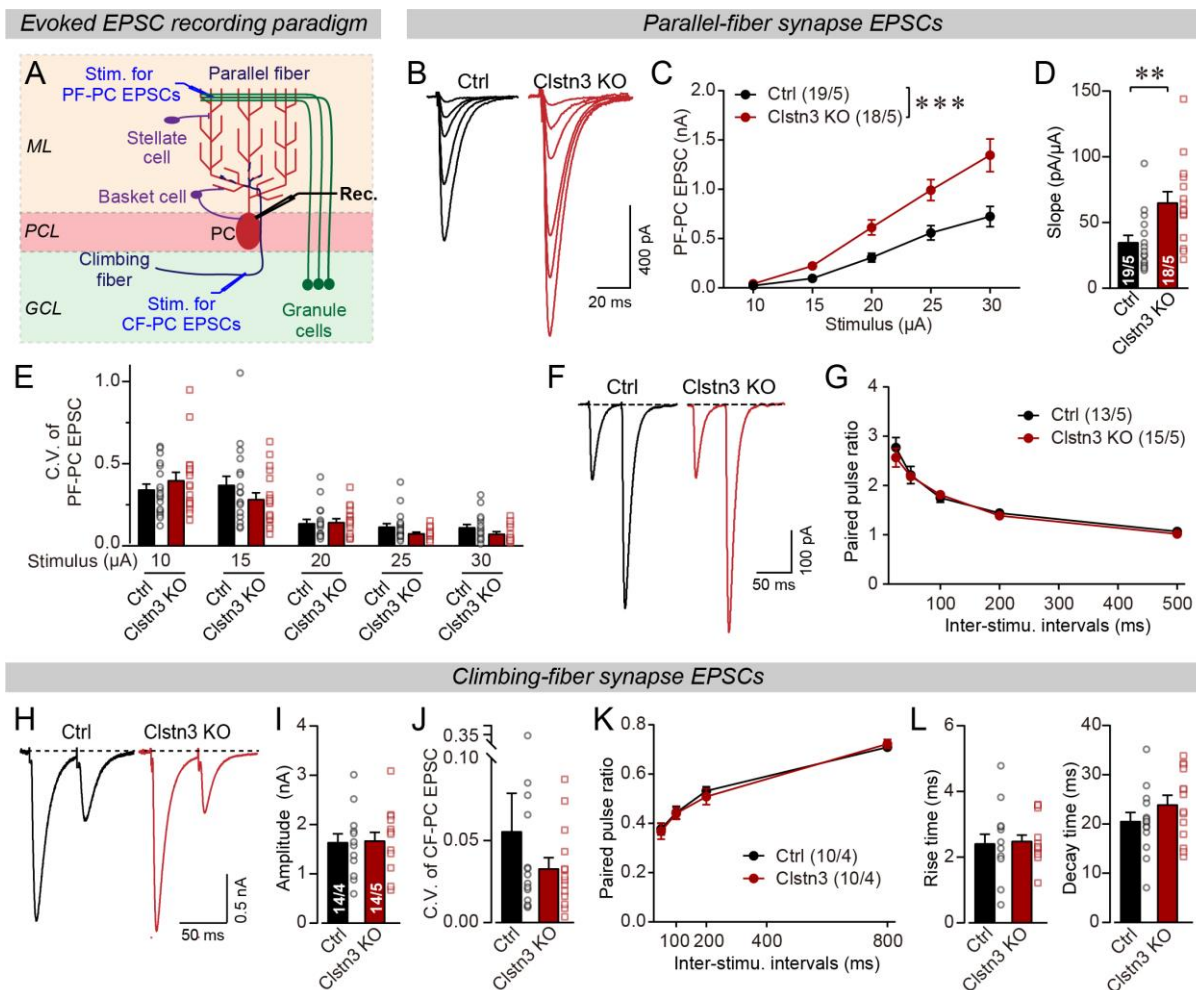
1065

Figure 9: *Clstn3* KO in Purkinje cells elevates parallel-fiber synaptic strength, while leaving climbing-fiber synaptic strength unchanged

(A) Schematic of the recording configuration for monitoring evoked EPSCs induced by parallel-fiber (PF-PC) and climbing-fiber stimulation (CF-PC) in Purkinje cells.

(B-D) The postsynaptic *Clstn3* KO robustly increases the input/output relation of parallel-fiber synapses (B, representative traces; C, input/output curve; D, summary graph of the slope of the input/output curve determined in individual cells).

(E-G) The postsynaptic *Clstn3* KO in Purkinje cells has no effect on presynaptic release probability as assessed by monitoring the coefficient of variation of evoked EPSCs (E, separately analyzed for different stimulus strengths) or the paired-pulse ratio (F, sample traces; G, plot of the paired-pulse ratio of parallel-fiber EPSCs as a function of interstimulus interval).

(H-L) The *Clstn3* KO has no effect on the amplitude, coefficient of variation, paired-pulse ratio, or kinetics of climbing-fiber synapse EPSCs (H, representative traces of climbing-fiber EPSCs elicited with an interstimulus interval of 50 ms; I & J, amplitude (I) and coefficient of variation (J) of evoked climbing-fiber EPSCs; K, plot of the paired-pulse ratio of climbing-fiber EPSCs as a function of interstimulus interval; L, rise [left] and decay times [right] of evoked climbing-fiber EPSCs).

1084   All numerical data are means ± SEM. Statistical analyses were performed by two-way
1085   ANOVA followed by Tukey's post hoc correction (C, G, K; for C, $F_{(1, 150)}$=35.83, p<0.0001)
1086   or unpaired t-test for experiments with two groups (D, E, I, J, L), with *p<0.05, **p<0.01.
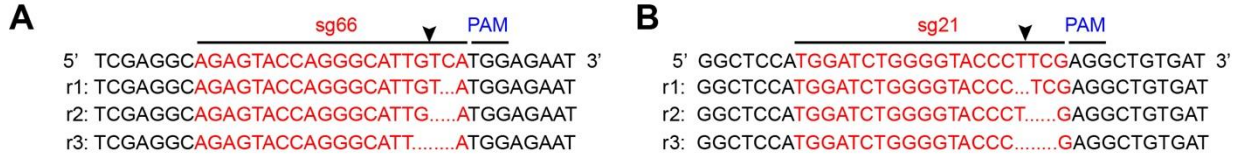
1087
SUPPLEMENTARY INFORMATION

1089
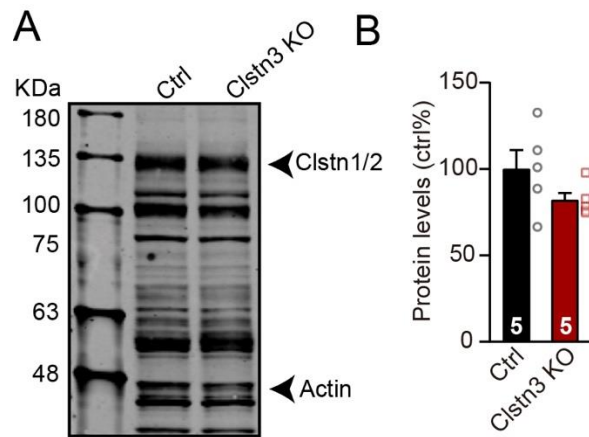
1090

Figure S1: CRISPR-mediated deletion of Clstn3 does not cause a major change in the levels of Clstn1/2 protein in cerebellum

(A) Representative immunoblot of cerebellar homogenates from mice that were stereotactically injected in the cerebellum with Clstn3 CRISPR-KO or control AAVs. Note that the antibody used has innumerable non-specific crossreactivities, but that the bands identified as representing the combination of Clstn1 and Clstn2 (Clstn1/2) were previously validated for this antibody (Um et al., 2014).

(B) Summary graph of the Clstn1/2 protein levels in control cerebellum and cerebellum with the Clstn3 KO. Data are means ± SEM (n = 5 mice). An unpaired t-test revealed no statistically significant difference between control and Clstn3 KO mice.

Potential genome editing pattern
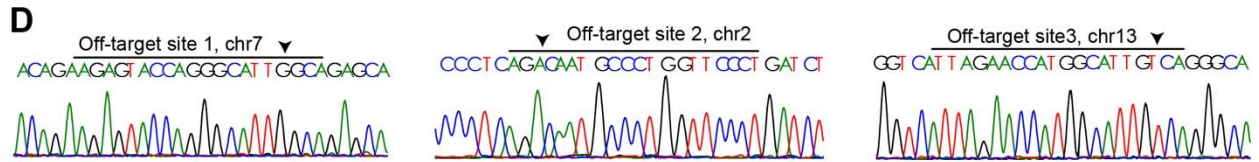
A

sg66 ▼ PAM

5' TCGAGGCAGAGTACCAGGGCATTGTCATGGAGAAT 3'
r1: TCGAGGCAGAGTACCAGGGCATTGT...ATGGAGAAT
r2: TCGAGGCAGAGTACCAGGGCATTG.....ATGGAGAAT
r3: TCGAGGCAGAGTACCAGGGCATT........ATGGAGAAT

B

sg21 ▼ PAM

5' GGCTCCATGGATCTGGGGTACCCTTCGAGGCTGTGAT 3'
r1: GGCTCCATGGATCTGGGGTACCC...TCGAGGCTGTGAT
r2: GGCTCCATGGATCTGGGGTACCCT......GAGGCTGTGAT
r3: GGCTCCATGGATCTGGGGTACCC........GAGGCTGTGAT

Sg66 potential off-target effects

C

Sg66 predicted off-target sites

No.	Chromosome	Strand	Position	Pattern	Type
1	chr7	1	143748794	AGAGTACCAGGGCATTGGCA	Intergenic
2	chr2	-1	167750018	AGGGAACCAGGGCATTGTCT	Intergenic
3	chr13	-1	34933982	TTAGAACCATGGCATTGTCA	Intergenic

D

Off-target site 1, chr7 ▼
ACAGAAGAGTACCAGGGCATTGGCAGAGCA

Off-target site 2, chr2 ▼
CCCTCAGACAATGCCCTGGTTCCCTGATCT

Off-target site3, chr13 ▼
GGTCATTAGAACCATGGCATTGTCAGGGCA

Sg21 potential off-target effects

E

Sg21 predicted off target sites

No.	Chromosome	Strand	Position	Pattern	Type
1	chr17	1	26570165	TGGATCTGGGCTACCCTTTG	Intergenic
2	chr5	-1	119991690	GGGAGCTGGTGTACCCTTCC	Intergenic
3	chr13	1	51347015	AGGATCTAGAGTACCCTTCA	Intergenic

F

Off-target site 1, chr17 ▼
CAGGTTGGATCTGGGCTACCCTTTGCAGCA

Off-target site 2, chr2 ▼
TGTTAGGGAGCTGGTGTACCCTTCCTAGGT

Off-target site 3, chr13 ▼
TTCTCAGGATCTAGAGTACCCTTCACAGCC
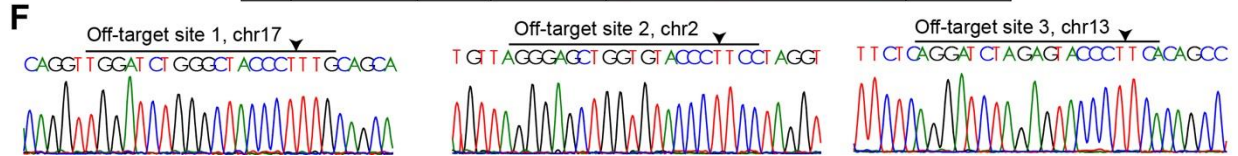
Figure S2: Predicted genome editing patterns by the sgRNAs used for the *Clstn3* KO in the current study and analysis of potential off-target effects of the sgRNAs using genomic sequencing of targeted *Clstn3* KO cerebellum

(A-B) Predicted genome editing effects for sg66 (A) and sg21 (B).

(C & D) The three top-ranked potential off-target sites for sgRNA66 as analyzed by sequence predictions (C), and their analysis by genomic sequencing of *Clstn3* KO cerebellum, demonstrating no obvious gene editing effects on all three sites (D). Arrow indicates potential cutting positions.

(E & F) Same as C & D, but for sgRNA21.
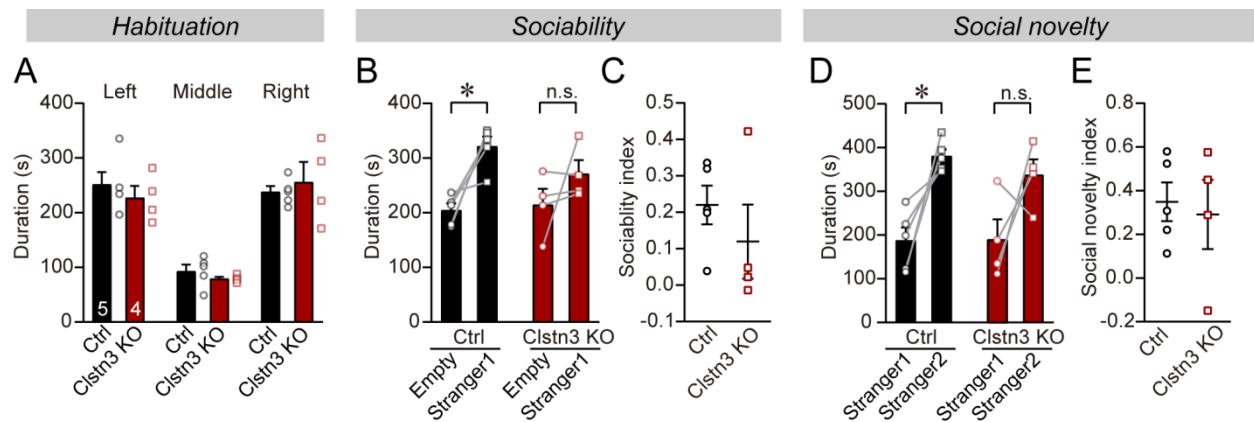
Figure S3: The *Clstn3* KO in the cerebellum does not significantly affect sociability and social novelty in mice as measured using the 3-chamber social behavior test

(A) Control and *Clstn3* KO mice exhibited the same exploration behavior of the left and right chambers during the habituation period.

(B & C) When exposed to a non-familiar 'stranger' mouse in one of the outer chambers, cerebellar *Clstn3* KO mice exhibited a lower degree of interactions with the stranger mouse but this was not statistically significant (B, the time that the test mouse spent in the chambers with empty cup or 'stranger1' mouse; C, sociability index).

(D & E) When given the choice between exploring a 'stranger 1' mouse to which it was previously exposed (see B), or a 'stranger 2' mouse that is novel, both control and cerebellar *Clstn3* KO mice prefer the novel mouse for interactions (D, the same as B, except empty cup has 'stranger2'; E, social novelty index).

All data are means ± SEM. Paired t-tests were applied to analyze the statistical significance of parameters within the same group, and unpaired t-tests to compare between control and Clstn3 KO groups at sociability index and social novelty index analysis, $*p<0.05$.
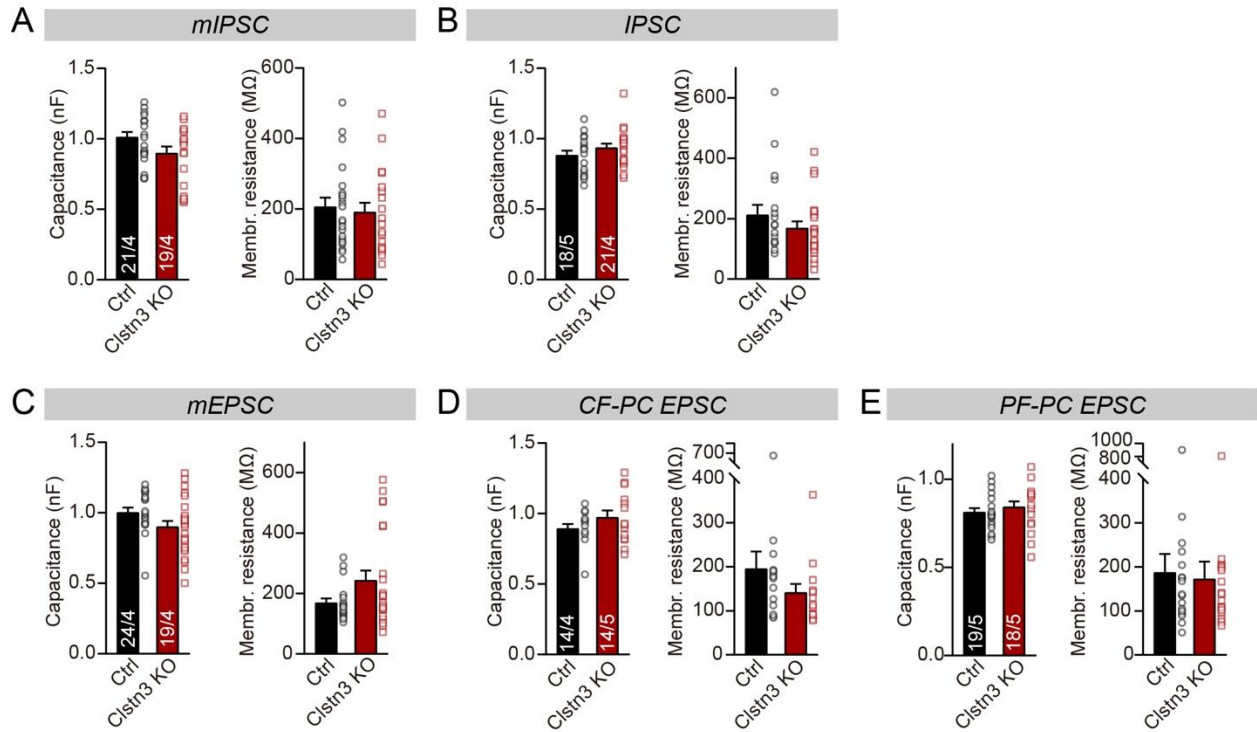
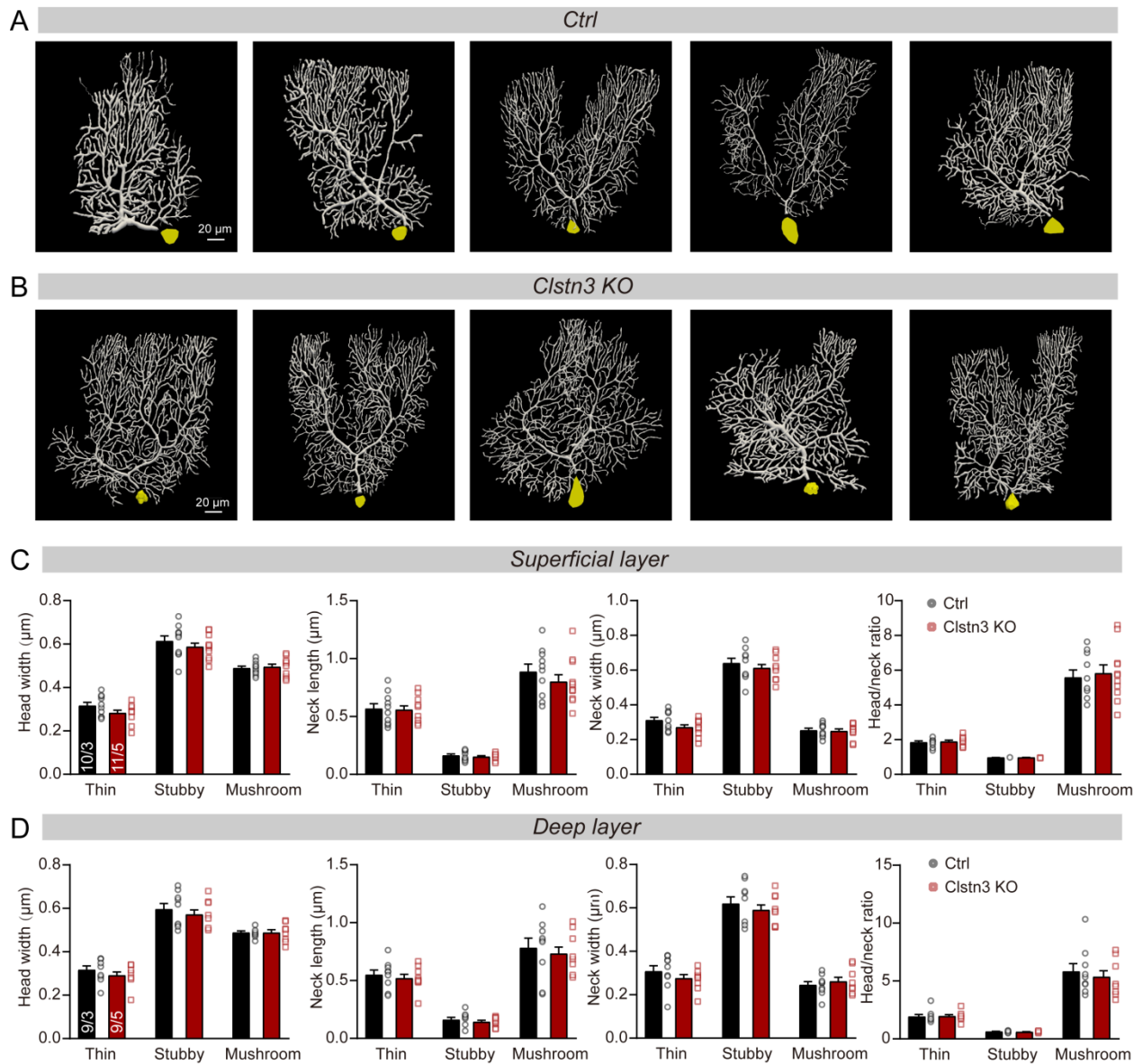**Figure S4: Capacitance and membrane resistance of Purkinje cells are unaffected by the *Clstn3* KO**

(A-E) Summary graphs of the capacitance (left) and input resistance (right) of Purkinje cells determined during the recordings described in Fig. 5 and 6. All data are means ± SEM. Statistical analyses were done with unpaired t-test, p>0.05.
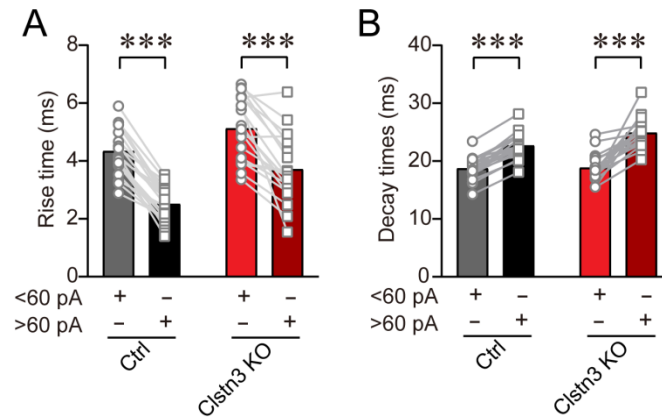
1133

Figure S5: Analysis of the kinetics of large (>60 pA) and smaller (<60 pA) mIPSCs confirm that larger mIPSCs that are presumably generated by basket-cell synapses closer to the soma have faster rise times but slower decay times

(A & B) Rise (A) and decay times (B) of large and smaller mIPSCs examined in the same Purkinje cells. All data are means ± SEM. Statistical analyses were performed with paired t-test, ***$p < 0.001$.
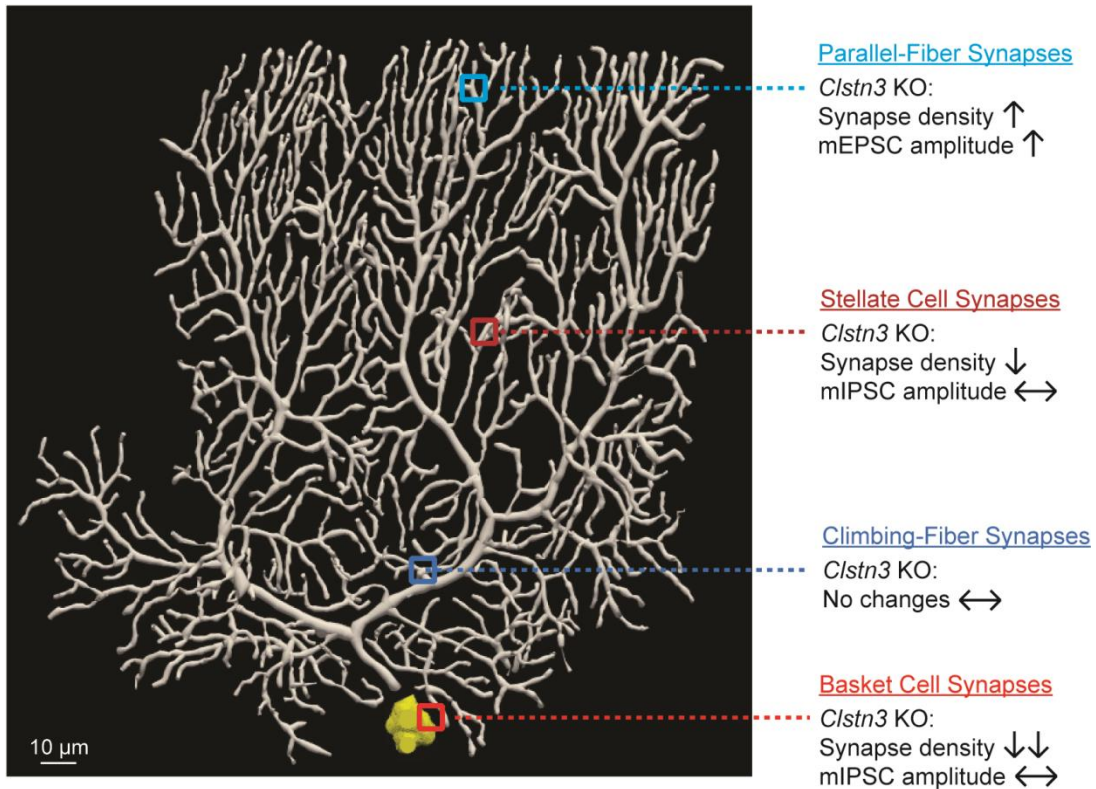
Figure S6: Images of individual reconstructed biocytin-filled Purkinje cells, and further quantifications of the morphological properties of spines from control and *Clstn3* KO Purkinje cells

(A & **B)** Images of all reconstructed Purkinje cells, as performed using Neurolucida360 software in control and *Clstn3* KO cerebellar cortex.

(**C** & **D)** Quantification of various spine parameters in the superficial (C) and deep layers (D) of control and *Clstn3* KO mice (left, head width; middle left, neck length; middle right, neck width; right, head/neck ratio). Data are means ± SEM. 5-8 spines were analyzed per layer per cell; the numbers of cells/mice examined are indicated in the left bar graph. Statistical analyses were performed with unpaired Student's t-tests, $p > 0.05$.

Parallel-Fiber Synapses
Clstn3 KO:
Synapse density ↑
mEPSC amplitude ↑

Stellate Cell Synapses
Clstn3 KO:
Synapse density ↓
mIPSC amplitude ↔

Climbing-Fiber Synapses
Clstn3 KO:
No changes ↔

Basket Cell Synapses
Clstn3 KO:
Synapse density ↓↓
mIPSC amplitude ↔

10 µm

1151

1152 **Figure S7: Summary of synaptic changes induced in Purkinje cells by the *Clstn3* KO.**
1153 The Purkinje cell image is from one of the cells reconstructed during the present study. The
1154 changes summarized on the right were identified in Figures 3-9.